Scalable fabrication of perovskite solar cells

Zhen Li[1], Talysa R. Klein[2], Dong Hoe Kim[1], Mengjin Yang[1], Joseph J. Berry[2], Maikel F. A. M. van Hest[2] and Kai Zhu[1] *

Abstract | Perovskite materials use earth-abundant elements, have low formation energies for deposition and are compatible with roll-to-roll and other high-volume manufacturing techniques. These features make perovskite solar cells (PSCs) suitable for terawatt-scale energy production with low production costs and low capital expenditure. Demonstrations of performance comparable to that of other thin-film photovoltaics (PVs) and improvements in laboratory-scale cell stability have recently made scale up of this PV technology an intense area of research focus. Here, we review recent progress and challenges in scaling up PSCs and related efforts to enable the terawatt-scale manufacturing and deployment of this PV technology. We discuss common device and module architectures, scalable deposition methods and progress in the scalable deposition of perovskite and charge-transport layers. We also provide an overview of device and module stability, module-level characterization techniques and techno-economic analyses of perovskite PV modules.

Hybrid organic–inorganic perovskites have emerged as a revolutionary class of light-harvesting materials. The general perovskite formula is ABX_3, in which A is a monovalent cation (such as methylammonium (MA^+), formamidinium (FA^+) or caesium (Cs^+)), B is a divalent metallic cation (such as Pb^{2+} or Sn^{2+}) and X is a halide (I^-, Br^- or Cl^-). After only several years of active research, the power conversion efficiency (PCE) of perovskite solar cells (PSCs) has substantially increased to more than 22%[1–4]. Remarkably, this high performance was achieved with a device that was fabricated through solution processing, which has not been demonstrated for other photovoltaic (PV) technologies. This makes PSCs promising candidates for a high-performance, low-cost PV technology. Several intrinsic material properties contribute to the demonstrated high efficiency of this new PV technology, such as high absorption coefficients, long carrier diffusion lengths, flexible bandgap tuning and defect tolerance[5–10]. However, for practical application, PV technologies need to be more than efficient — they also need to be stable and scalable.

During the past few years, we have seen remarkable progress towards future large-scale PSC manufacturing using scalable deposition. There has been a rapid improvement in the efficiency of PSCs at different size scales (FIG. 1a) — namely, small-area cells (~0.1 cm²), large-area cells (~1 cm²) and modules (>10 cm²). The surge in performance of small-area devices is largely ascribed to the improved composition and morphology of perovskite thin films owing to innovations in solution chemistry and the fabrication process. These developments have been readily transferred to large-area devices, resulting in an increase in efficiency that has closely followed the trend of small-device development. By contrast, the efficiencies of PSC modules notably lag behind those of single-cell devices.

A loss in efficiency is inevitable when the solar cell or module area increases. This loss is the result of a combination of several factors, including higher series resistance, lower shunt resistance, non-uniform coating over a large area and the unavoidable dead (that is, inactive) area of bus bars and interconnections. FIGURE 1b shows the correlation between the state-of-the-art PCE and the solar cell or module area for different types of solar cells: silicon, cadmium telluride (CdTe), copper indium gallium selenide (CIGS), dye-sensitized solar cell (DSSC), organic PV (OPV) and a PSC. The different types of solar cells (except for the PSC) all follow an apparent inverse scaling law, with the absolute PCE value decreasing by about 0.8% when the device area increases by an order of magnitude. The current status of PSC modules falls below this predicted trend: there is a greater decrease in efficiency when the PSC area increases compared with other types of solar cells. This disparity in efficiency undoubtedly results from the minimal research efforts on the scaling of PSCs.

[1]*Chemistry and Nanoscience Center, National Renewable Energy Laboratory.*
[2]*Materials Science Center, National Renewable Energy Laboratory, Golden, CO, USA.*

*e-mail: Kai.Zhu@nrel.gov
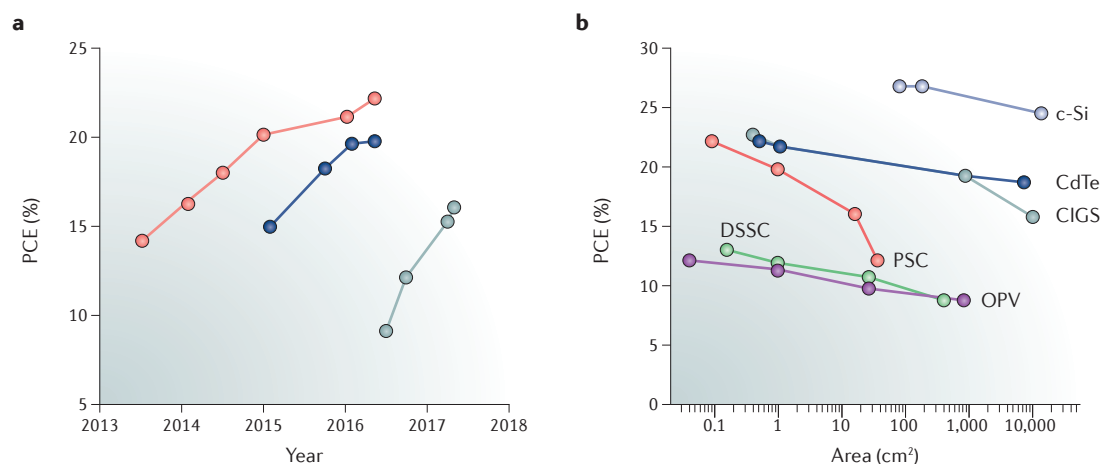
Figure 1 | **Efficiency of perovskite solar cells. a** | In the past few years, there has been a rapid increase in the power conversion efficiency (PCE) of perovskite solar cells (PSCs) with different device areas: small-area cells (pink), large-area cells (blue) and modules (grey). **b** | The plot shows how the device area affects the PCE of different types of solar cells[3,4,13,15,62,197,230,231]. CdTe, cadmium telluride; CIGS, copper indium gallium selenide; c-Si, crystalline silicon; DSSC, dye-sensitized solar cell; OPV, organic photovoltaic.

Challenges in scaling up PSCs include developing scalable deposition strategies for the uniform coating of all device layers over large-area substrates, including the perovskite photoactive layer, electron-transport layer (ETL), hole-transport layer (HTL) and electrodes; achieving better control of film formation across the device stack at large scales by improving the precursor chemistry to better match the processing methods; and developing procedures for fabricating and integrating perovskite modules, as well as understanding the impact of device architecture on the performance of the module interconnections and the reliability and stability of module operation.

Despite numerous challenges, the progress made towards scaling up PSCs is impressive. Small-area laboratory devices fabricated by scalable deposition (for example, by blade coating) have already reached PCE levels close to those fabricated by spin coating[11–13]. Although the PCE of perovskite modules still lags behind that of smaller devices, the rate of increase in the PCE of perovskite modules is unprecedented compared with other PV technologies[14] (FIG. 1a). A perovskite module with a certified PCE of 16% and an area >16 cm^2 has recently been demonstrated[15].

In this Review, we focus on the key considerations for scaling PSCs and on the challenges for transitioning from the laboratory scale to the factory scale. We summarize common PSC and module architectures and then discuss efficiency losses that occur on moving from cells to modules as well as the importance of module design for achieving efficiency and stability. We compare various scalable deposition methods, including both solution-phase and vapour-phase depositions, their advantages and limitations with respect to PSC processing and the current status of the corresponding efforts to scale up PSCs. We provide an overview of recent progress in solution chemistry and processing control towards the scalable deposition of perovskite and charge-transport layers along with characterization

techniques suitable for large-area perovskite absorber layers and module structures. Advances in the fabrication and characterization of large-area devices have greatly contributed to recent progress in scaling. Stability and cost are important issues to be addressed before PSCs can be commercialized. We discuss the strategies for improving the stability of PSCs and potential reliability issues facing PSC modules. Additionally, current reports on manufacturing cost analyses and life cycle assessments based on common PSC or module structures are summarized. Finally, we provide an outlook on the challenges associated with PSC scaling, with a focus on the scalability of processes and materials.

Device architectures
Perovskite solar cell architectures
The most common device architectures for PSCs can be categorized into three types: mesoporous n–i–p, planar n–i–p and planar p–i–n (FIG. 2a).

The mesoporous n–i–p architecture was the first device architecture to be developed and has evolved notably from the early days of PSC research. A typical mesoporous PSC comprises an ETL scaffold with nanoscale pores. A perovskite absorber layer covers the scaffold, forming a compact capping layer and also penetrating into the scaffold, leading to an intermixed layer. The HTL and the top electrode are then sequentially deposited on the perovskite layer to complete the device stack. The mesoporous layer can facilitate charge separation and help suppress the notorious photocurrent–voltage (J–V) hysteresis phenomenon in PSCs[16]. A record PCE of 22.1% has been attained with a mesoporous structure[3].

The planar n–i–p architecture contains a compact ETL layer and thus does not feature the perovskite–ETL intermixed layer that is present in the mesoporous architecture. Although the planar structure is more prone to exhibiting J–V hysteresis, recent optimization of the ETL/perovskite interface has given rise to

high-performance planar PSCs that show little hysteresis[17–21]. In this context, the mesoporous layer adds one more step to the fabrication process, which is perhaps unfavourable for scaling. It remains to be seen if the mesoporous scaffold is indispensable for achieving higher PCE or improved stability. It is worth noting that for certain n–i–p device architectures, the HTL layer can be eliminated by using carbon or gold electrodes[22–24].

The planar p–i–n architecture is generally referred to as an inverted structure because the carrier extraction layers are inverted with respect to the n–i–p structure. Devices with a p–i–n architecture are often constructed with a planar structure with a compact HTL.

Perovskite solar modules

As with other thin-film PV technologies, it is not practical to fabricate a single PSC on a large-area substrate because the parasitic resistance loss in the transparent conducting electrode is substantial over a long transport distance. Resistance losses can be managed by dividing a large cell into smaller sub-cells with series interconnections to form a module[25] (FIG. 2b). The series interconnections sum the voltage available from the module. The interconnections occupy ~3–10% of the module area, depending on the geometry of the interconnection layout. The interconnection area is inactive for power generation and thus is a major source of power loss in PV modules. The ratio between the photoactive area and the total area of a module is defined as the geometric fill factor (GFF) of the module. Modules with a higher GFF can generate more power for a given module size. Thus, a well-accepted practice for reporting module efficiency for conventional PV materials is to report the efficiency of a designated illumination area (or aperture area) that should include all interconnections[26] (FIG. 2c). However, some perovskite module efficiencies are reported as the efficiencies limited to the active area, which excludes the area of the interconnections. In such cases, it is important to also report the GFF so that results can be accurately compared. For example, a module with an active-area efficiency of 15% and a GFF of 80% has an aperture efficiency of 12%.

Thin-film PV modules (for example, CdTe and CIGS) are generally fabricated by first depositing the thin-film materials on one substrate and then separating individual cells by laser or mechanical scribing. There are three separation processes involved in module fabrication (FIG. 2b). In the first step, the bottom conducting electrode (for example, transparent conductive oxide (TCO)) is divided into parts to form isolated substrates for the individual sub-cells; in the second step, some of the active material (ETL, perovskite and HTL) is
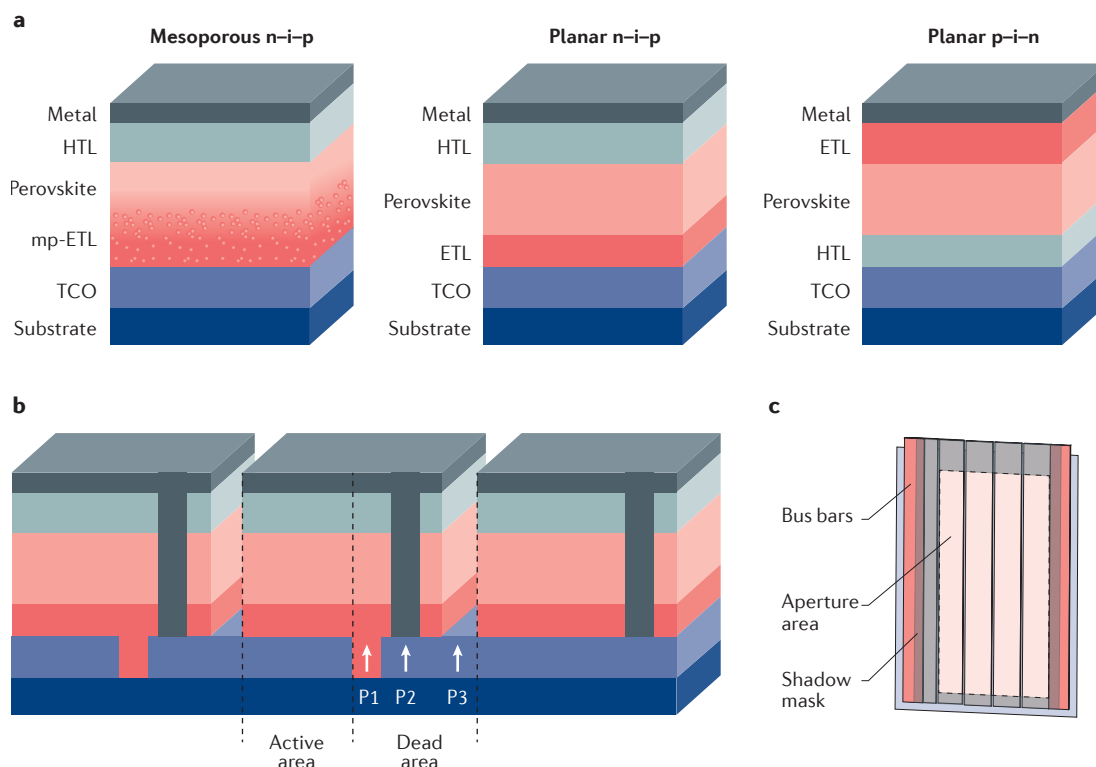
Figure 2 | **Perovskite solar cell and module architectures. a** | Schematics showing the layered structures of three typical perovskite solar cell architectures: mesoporous n–i–p, planar n–i–p and planar p–i–n. **b** | Interconnection of a perovskite module fabricated by typical scribing processes for thin-film solar modules. The P1 scribe separates the bottom TCO substrate, the P2 scribe provides a channel to connect the top contact of one cell to the bottom contact of the next cell to form the interconnection, and the P3 scribe isolates the top metal contact between neighbouring cells. **c** | Performance measurement setup for solar cell modules with a shadow mask. The module efficiency should be reported on the basis of the aperture area, including the dead area of interconnects. ETL, electron-transport layer; HTL, hole-transport layer; mp-ETL, mesoporous ETL; TCO, transparent conductive oxide.

removed to construct interconnections between the sub-cells; and in the final step, the top electrodes and the edge of the module are isolated to separate the individual sub-cells and to define the outer boundaries of the module. PSCs can be processed into modules with a similar fabrication scheme. Scribing with lasers is highly desirable for industrial production, with the advantages of low cost, fast production rate and high GFF, which is associated with high precision and fine resolution. Perovskite modules fabricated through all-laser scribing have demonstrated a GFF of 94%[25]. However, perovskite materials are typically more thermally sensitive than other thin-film solar cell materials. Thus, one possible drawback of laser scribing is the potential for degradation and/or redeposition of materials near the scribe. Optimizing the sub-cell separation and module interconnection procedures for perovskite modules is important for scaling up PSCs and needs to be researched further.

Another fabrication scheme for module assembly is to deposit each layer only at desired areas, thus requiring no additional scribing to form the interconnections. Such on-demand deposition can be realized through patterned printing and deposition with masks. However, patterned deposition requires pattern alignment for each layer to be deposited, and the spatial resolution is typically lower than with laser scribing. Thus, modules fabricated with this method normally exhibit a lower GFF and larger dead-area power loss.

Scalable deposition methods

To deposit perovskite films through solution processing, organic halides and lead halides are first dissolved in organic solvents such as N,N-dimethylformamide (DMF), dimethyl sulfoxide (DMSO) and γ-butyrol-actone (GBL). These perovskite precursor solutions are used in both spin coating and scalable deposition methods. Spin coating is the most common method for perovskite thin-film deposition. However, it is generally limited to a scale of <10 cm, and a large portion (>90%) of the precursor ink is wasted in the process. Modules can be fabricated by spin coating on a substrate area of up to about 10 cm × 10 cm but with a considerably lower PCE than their smaller-area counterparts[27]. In spin coating, thinning and smoothing of the wet-solution films rely on the continuous centrifugal force from spinning, which is difficult to replicate in scalable deposition processes. Thus, the solution chemistry and processing conditions developed for spin coating cannot be easily applied in other scalable deposition methods. Furthering our understanding of the factors that affect thin-film formation and increasing our control of thin-film formation in different deposition processes are crucial for scaling up PSCs.

Scalable solution deposition methods

Scalable solution deposition methods for perovskite growth include, but are not limited to, blade coating, slot-die coating, meniscus coating, spray coating, inkjet printing, screen printing and electrodeposition. Here, we briefly compare these deposition methods as well as their use for PSC cell and module development.

Blade coating. In the blade-coating deposition method, a blade is used to spread precursor solution on substrates to form wet thin films (FIG. 3a). The film thickness is generally controlled by several factors, including the concentration of the precursor ink, the gap between the blade and substrate, and the speed at which the blade moves across the substrate. This technique can be adapted for continuous fabrication with roll-to-roll setups, in which the blade is stationary and flexible substrates on a roller are in motion. The ink waste is substantially reduced compared with spin coating, especially in continuous roll-to-roll deposition. PSCs fabricated by blade coating have demonstrated PCEs >19%[11,12].

Slot-die coating. Slot-die coating (FIG. 3b) is similar to blade coating and uses an ink reservoir with a thin slit to apply ink over the substrate. Ink flow can be better controlled in slot-die coating, but this method normally requires larger quantities of ink to fill the ink reservoir and supply pipe and thus is generally less suitable for use in the development of new ink chemistries. As a result, slot-die coating has been less explored, and at present, the resultant PSCs have a much lower PCE than those fabricated through blade coating. However, slot-die coating shows better yield and reproducibility than blade coating when the ink is already fully developed. Thus, it has more potential to be applied in roll-to-roll fabrication in the future. It is noteworthy that both blade and slot-die coating use a moving meniscus liquid edge of precursor ink to spread the liquid film across the substrate. Some other non-conventional methods to create the meniscus edge are pulling a substrate out of a precursor ink (for example, dip coating)[28] and sheering a cover plate over the deposition substrate[29]. A recently reported soft-cover coating method also uses a meniscus edge for perovskite deposition. Before coating, a soft polymer sheet covers the coating substrate and traps the precursor ink between the layers. The meniscus liquid edge is formed and then moved as the polymer sheet is gradually peeled off. Uniform perovskite thin films of up to 51 cm^2 have been deposited using this soft-cover method[30].

Spray coating. In spray coating, a nozzle is used to disperse tiny liquid droplets onto substrates (FIG. 3c). Spray coating can be further classified according to the method used for generating droplets, such as pneumatic spraying (through fast gas flow), ultrasonic spraying (through ultrasonic vibration) or electrospraying (through electrical repulsion). Pneumatic spraying and ultrasonic spraying are commonly used for compact oxide layer deposition in PSCs. The perovskite layer can also be deposited by ultrasonic spraying[31–35]. Droplet size and placement are random in the spraying process, and several droplets need to overlap in a local area to ensure full coverage. Furthermore, new droplets can dissolve the already deposited materials, adding to the processing complexity. Keeping the substrate at an elevated temperature during spraying increases the rate of solvent evaporation and suppresses the redissolution of deposited material. The balance between solvent removal and material redissolution can be controlled
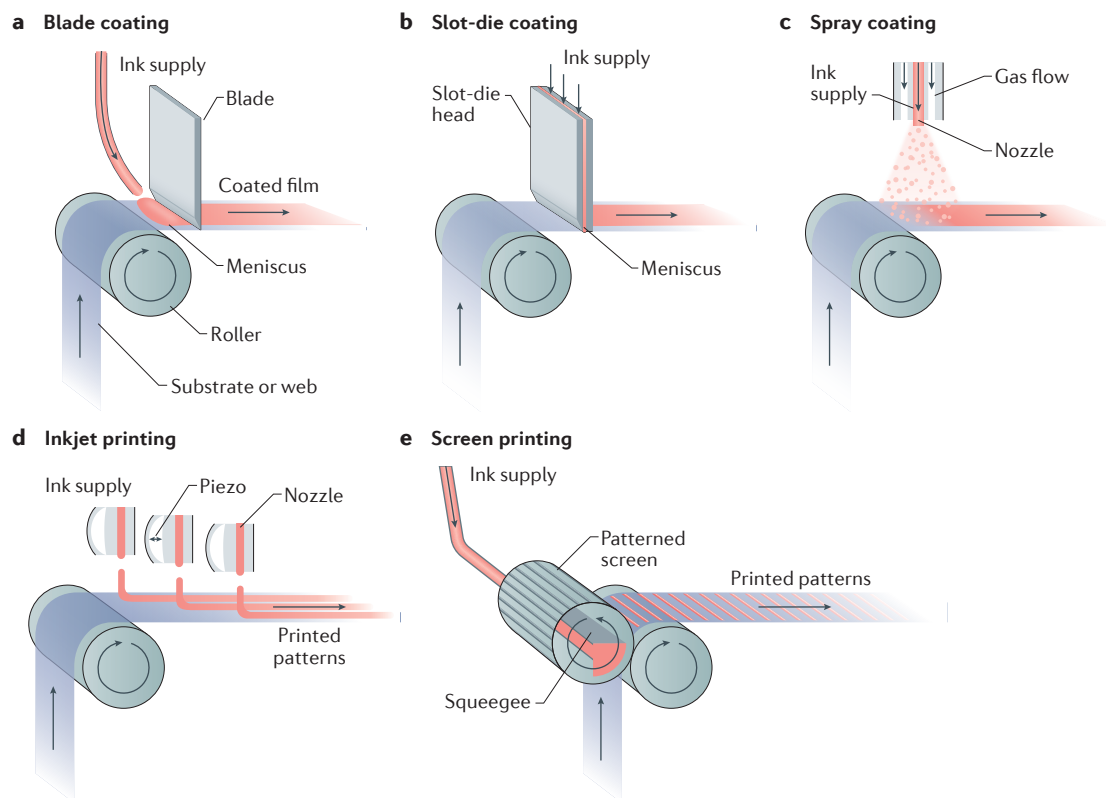
Figure 3 | **Common scalable solution deposition methods for the roll-to-roll fabrication of perovskite solar cells.** Scalable methods for perovskite deposition include blade coating (panel **a**), slot-die coating (panel **b**), spray coating (panel **c**), inkjet printing (panel **d**) and screen printing (panel **e**).

by carefully tuning the solvent ratio and substrate temperature[34]. Electrospraying applies a high voltage between the spray nozzle and substrate. The droplets are smaller with electrical repulsion, and the electric field also increases the impact velocity of the droplets and the extent to which the droplets spread on substrates[36].

Inkjet printing. In inkjet printing, nozzles are used to disperse the precursor ink, with fine control of the droplet size and trajectory (FIG. 3d). Miniaturized nozzles and a short distance between the nozzles and substrate enable ultrafine lateral resolution, as demonstrated in digital printers. This patterning ability is suitable for printing electronics. Small-area PSCs (0.04 cm²) have been fabricated using inkjet printing[37]. However, whether inkjet printing is suitable for the high-volume, large-area production of perovskite solar modules will depend on the printing speed and device structure.

Screen printing. In screen printing, a patterned mesh screen is used to hold and transfer ink to the substrate (FIG. 3e). This method has good patterning ability with a lateral resolution of ~75–100 μm (REF. 38). The unwanted area of the mesh screen is blocked by the exposed photosensitive polymer emulsion, and the open holes of the mesh hold the viscous ink as a squeegee spreads ink across the screen. The ink is then transferred to the substrate to form the desired pattern. The thickness of the resulting film is determined by the mesh size and

thickness of the emulsion layer. Screen printing is usually used to deposit thicker films (~1–10 μm), and it has been used to fabricate mesoporous scaffolds and carbon back electrodes in PSCs[22,39].

Electrodeposition. Electrodeposition is another scalable solution deposition method to deposit thin films over a large area. There are no reports of the direct deposition of halide perovskites using electrodeposition, and it generally takes two steps to deposit perovskite thin films by electrodeposition. First, PbO_2 or PbO is electrodeposited on a conducting substrate. The lead oxide is then converted into a perovskite through reaction with organic halides[40] or reaction with HI acid to form PbI_2, which is then converted into a perovskite[41–44]. The advantage of electrodeposition is the use of a non-toxic solvent (usually an aqueous solution) in the process.

TABLE 1 summarizes different scalable deposition methods for preparing large-area perovskite thin films and their status in depositing charge-transport layers. Their roll-to-roll and patterning capabilities are also compared, together with the current state-of-the-art device performance for both single cells (aperture area ≤1 cm²) and modules (aperture area ≥10 cm²). Note that the certified record efficiency for a perovskite module (16.0%) is not listed here because the deposition method is not disclosed in the report[15]. A continuous fabrication line of PSCs may use multiple deposition techniques integrated together. Other deposition techniques have

also been demonstrated for perovskite deposition, such as brush coating[45], dip coating[28,46] and air-knife-assisted coating[47].

Vapour-phase deposition

Vapour-phase deposition is common in solar cell fabrication: the deposition of CIGS and CdTe relies heavily on physical vapour deposition (PVD), and the doping of silicon is realized through chemical vapour deposition (CVD). A PVD apparatus for the large-scale fabrication of solar cells has been developed and successfully applied, and this experience and equipment have been readily translated to PSC fabrication. Perovskite thin films have been deposited with both PVD and CVD methods. PVD refers to the process in which a perovskite or its precursor is directly sublimated to form a perovskite thin film, whereas CVD refers to the process in which a lead halide is converted into a perovskite using organic halide vapours.

The deposition of perovskite thin films using a PVD method was first demonstrated in 2013 (REF. 48). Uniform and compact $MAPbI_{3-x}Cl_x$ thin films were obtained by the co-evaporation of $PbCl_2$ and methylammonium iodide (MAI), enabling the construction of efficient planar PSCs. Ultrathin (50 nm) and large-area (5 cm × 5 cm) perovskite films, which are usually difficult to obtain by a solution method, were achieved using thermal evaporation[49]. In addition, PVD is a solvent-free method and largely independent of the substrate, making it attractive for the fabrication of perovskite–perovskite tandem devices. For example, an efficient $MA_{0.5}FA_{0.5}Pb_{0.75}Sn_{0.25}I_3/MAPbI_3$ tandem device was fabricated by using solely thermal evaporation to directly deposit the $MAPbI_3$ sub-cell on the low-bandgap cell $(MA_{0.5}FA_{0.5}Pb_{0.75}Sn_{0.25}I_3)^{[50]}$.

The first CVD method developed for the deposition of perovskite materials involved the reaction of PbI_2 thin films with MAI vapour[51]. More CVD systems have been demonstrated with different chamber configurations and designs, environmental pressures, reaction temperatures and organic halide sources[52–54]. Towards the scaling of PSCs, CVD conversion has been used to deposit $FAPbI_3$ thin films on 5 cm × 5 cm substrates and to fabricate 12 cm² modules with a PCE of 9%[52].

Although vapour-phase deposition has the potential to be used to deposit perovskite thin films over large areas, these methods usually require more sophisticated vacuum equipment and longer processing times, which could potentially hinder their application for the low-cost fabrication of PSCs.

Scaling up the absorber layer

Nucleation and crystal-growth control

The performance of PSCs depends greatly on the morphologies of the perovskite absorber layer. Scaling up PSCs requires coating perovskite thin films uniformly over large-area substrates without pinholes or other inhomogeneities. In an uncontrolled drying process, perovskite crystals tend to have preferential growth and form thin films with dendritic structures[55], leading to poor surface coverage on the substrates and thus the formation of shunted paths in the solar cells. Strategies proposed to control nucleation and crystal growth to circumvent dendrite formation include physical approaches to promote supersaturation and chemical additives to control crystal growth (FIG. 4). By applying these strategies, smooth and compact perovskite thin films that are suitable for large-area PSCs have been demonstrated.
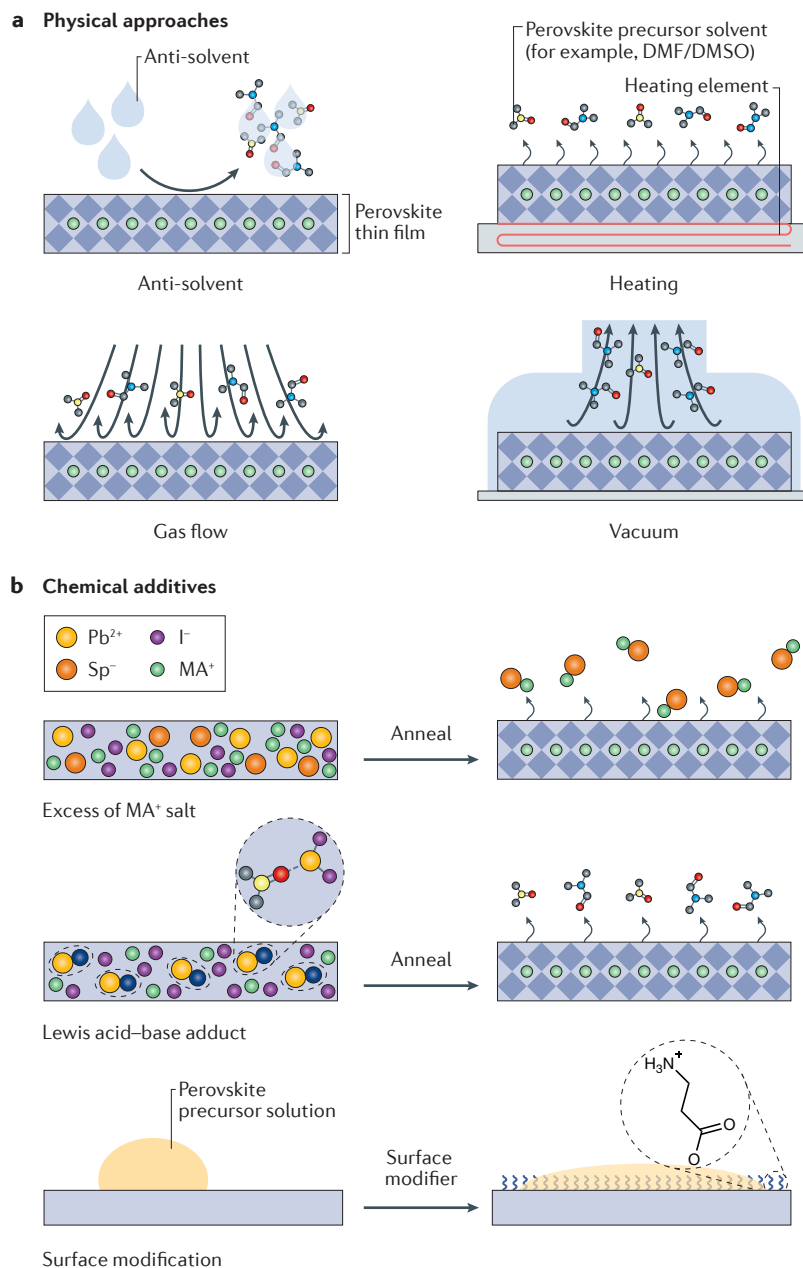
Physical approaches to promote supersaturation. Rapid solvent removal from perovskite precursor solutions increases the supersaturation, leading to more nucleation and shorter grain growth times. A shorter growth time reduces the migration of the solute in the solution. Coupled with more nuclei, a shorter growth time suppresses the overgrowth of individual nuclei to form large dendritic structures. The rapid removal of solvent can be realized by anti-solvent extraction[16,56,57], heating[46,58,59], forced gas flow[47,60,61], vacuum-assisted drying[62–64] or a combination of these physical approaches[65] (FIG. 4a).

Anti-solvent extraction is commonly used to achieve smooth, compact perovskite thin films. The anti-solvents need to be miscible with the solvents used to dissolve the perovskite precursors, but the perovskite itself should not be soluble in the anti-solvent. Using anti-solvents to extract solvents from the precursor solutions can lead to rapid supersaturation of the perovskite precursor film and fast precipitation of the perovskite materials. Examples of anti-solvents include toluene[16], chlorobenzene[56], ethyl ether[57], ethyl acetate[66], hexane[67] and anisole[68]. Anti-solvent extraction has been combined with spin-coating deposition by dripping the anti-solvent onto a spinning substrate covered with a perovskite precursor solution[16]. However, dripping anti-solvent during spin coating produces complex dynamics across the substrate, and more uniform results can be achieved by spraying the anti-solvent[69]. Anti-solvent spraying was used to fabricate a 16 cm²

Table 1 | **Comparison of scalable solution processing methods for perovskite solar cells**

Method	Roll-to-roll?	Pattern?	Demonstration in device stack	State-of-the-art device performance	
				Single cell[a] (%)	Module[b,c] (%)
Blade coating	Yes	No	• Perovskite[11,12,59,71,83,223] • ETL[83] • HTL[83]	19.5 (REF. 12)	14.1 (REF. 11) (GFF = 0.88)
Slot-die coating	Yes	Yes[d]	• Perovskite[61,84,106,165] • ETL[61,84,106,165] • HTL[61,84,106,165]	14.7 (REF. 165)	–
Spray coating	Yes	Yes	• Perovskite[31–36] • ETL[35,224] • HTL[35]	18.3 (REF. 34)	15.5 (REF. 34) (GFF = 0.4)
Inkjet printing	Yes	Yes	• Perovskite[37,225]	12.3 (REF. 37)	–
Screen printing	Yes	Yes	• ETL[39,173] • HTL[226]	15.6 (REF. 227)	10.8 (REF. 174) (GFF = 0.7)
Electrode position	No	No	• Perovskite[40–44] • ETL[228,229] • HTL[161]	14.6 (REF. 43)	–

ETL, electron-transport layer; GFF, geometric fill factor; HTL, hole-transport layer. [a]The single cells have aperture areas ≤1 cm². [b]The modules have aperture areas ≥10 cm². [c]The power conversion efficiency (PCE) of a module is based on the active-area efficiency, $PCE_{aperture} = PCE_{active} \times GFF$. [d]1D patterning.

a Physical approaches

Anti-solvent

Perovskite thin film

Anti-solvent

Perovskite precursor solvent (for example, DMF/DMSO)

Heating element

Heating

Gas flow

Vacuum

b Chemical additives

Pb²⁺   I⁻   Sp⁻   MA⁺

Excess of MA⁺ salt   Anneal

Lewis acid–base adduct   Anneal

Perovskite precursor solution

Surface modification   Surface modifier

Figure 4 | **Strategies to control nucleation and film formation for scaling up perovskite absorber layers. a** | Physical approaches to promote supersaturation include the use of an anti-solvent, heating, gas flow or vacuum-assisted drying to rapidly remove solvents from the perovskite precursor solution. **b** | Chemical additives can be used to control crystal growth. Examples of additives include excess methylammonium (MA⁺) salts and Lewis bases (for example, DMSO), which form complexes with perovskites and modify the resulting film morphologies. Surface modification with a self-assembled monolayer can be used to increase solution wetting on substrates and improve film morphology. DMF, N,N-dimethylformamide; DMSO, dimethyl sulfoxide; Sp⁻, spectator anion.

perovskite single cell with a PCE of 12.1%[70]. However, anti-solvent dripping and spraying have been deployed only with spin coating, and they are difficult to implement in scalable deposition. To address this challenge, anti-solvent bathing has been developed, in which the precursor film is soaked in a bath of anti-solvent for a short period of time[57]. In principle, anti-solvent bathing places no limit on the substrate size and could be incorporated in roll-to-roll continuous fabrication.

Heating can also expedite solvent removal in the solution processing of perovskite thin films. For example, a hot-casting technique has been used to deposit perovskite films[58]. In this hot-casting process, a hot perovskite precursor solution (70 °C) was spin-coated on hot substrates (180 °C), forcing the solvents to rapidly evaporate. Because heating the substrate during large-area deposition is rather easy, this heating approach has been used to control the perovskite film morphology in blade coating, spray coating, dip coating and soft-cover coating[12,28,30,31,34,59,71,72]. For example, a pinhole-free perovskite thin film was obtained by heating the substrate close to the boiling point of the perovskite precursor solvent during blade coating[59]. Moreover, a hot dip-coating technique has been developed, in which hot substrates were dipped into a perovskite precursor solution and then drawn out, forming perovskite thin films in 2 s (REF. 46).

Forced gas flow and vacuum-assisted drying have also been used for rapid solvent removal. A forced gas flow was first used to induce fast crystallization during spin coating[60]. This concept was later adapted for slot-die coating, using an air blade to assist solvent drying[61]. A vacuum flash-drying method that uses a vacuum to extract solvent has also been reported. With the vacuum-assisted drying technique, large-area PSCs (>1 cm²) with PCEs >20% were achieved[62]. In a further development, an apparatus was designed to simultaneously apply a low pressure and strong gas flow over the wet substrate; the combined effect of the gas flow and vacuum increased the solvent removal rate[65].

Recently, solvent systems with ultrafast evaporation rates have been reported for perovskite deposition. Methylamine (CH_3NH_2) gas can considerably increase the solubility of MAI and PbI_2 in solvents by forming MAI–mCH_3NH_2 ($m \leq 3$) and PbX_2–nCH_3NH_2 ($n \leq 1$) complexes[13]. Assisted by methylamine gas, perovskite precursors can be dissolved in normally poor perovskite solvents, such as acetonitrile. For example, in one study, methylamine gas was dissolved in acetonitrile, and this combined system was then used to dissolve a perovskite. The solvent evaporated quickly during spin coating of the perovskite precursor solution, facilitating fast crystallization of the perovskite at room temperature with an initial device reaching a PCE >18%[73]. Although this solvent system has so far been used only in spin coating, it should be applicable to large-scale deposition techniques, such as blade or slot-die coating. With an excess of methylamine gas, the $MAPbI_3$–CH_3NH_2 complex is liquid under ambient conditions[74]. The $MAPbI_3$–CH_3NH_2 liquid can be processed through solution methods and, as the excess methylamine can be rapidly removed, results in fast crystallization of the perovskite. This approach can be used to fabricate large-area devices; for example, a soft cover under high pressure was used to spread $MAPbI_3$–CH_3NH_2 liquid and to attain a uniform $MAPbI_3$ film over a large substrate (8 cm × 8 cm). A perovskite module fabricated with this method reached a certified aperture PCE of 12.1% (~90% GFF)[13].

Chemical additives to control crystal growth. Nucleation and crystal growth are also strongly influenced by the chemistry of the perovskite precursors. The morphology of perovskite thin films can be tuned by varying the chemical composition or by introducing additives to the precursor solution (FIG. 4b). For example, perovskite thin films derived from a chloride-containing precursor ($PbCl_2 + 3MAI$) showed better coverage and had a larger grain size than those obtained from a stoichiometric precursor ($PbI_2 + MAI$)[75]. Other chloride additives (for example, MACl or NH_4Cl) can also be used to prepare chloride-containing perovskite precursors, generating thin films with a morphology similar to those obtained with $PbCl_2$ (REFS 76–78). It is generally believed that Cl^- competes with I^- to coordinate to Pb^{2+}, suppressing the formation of Pb–I–Pb plumbates and nuclei in the solution[55,79]. Chloride-containing additives slow nucleation and crystal-growth processes but also induce the formation of a chloride-containing intermediate phase after the solvent is removed. The film with an intermediate phase is less crystalline than a perovskite film directly deposited from a stoichiometric precursor ($PbI_2 + MAI$), but it is usually less rough, with no dendrites or pinholes. The film compactness is preserved when the intermediate phase is transformed into the perovskite through the subsequent chemical reaction[80,81]. Chloride-containing non-stoichiometric precursors are often used in the spray, blade and slot-die coating of perovskite thin films[34,61,82–84].

In addition to chloride additives, other organic halides and $Pb(CH_3CO_2)_2$ can be used as additives to induce the formation of an intermediate phase for growing uniform perovskite films[85,86]. A general reaction scheme for the conversion of the intermediate phase to the perovskite ($MAPbI_3$) has been proposed:

$$PbSp_2 + 3MAI \rightarrow (MAPbI_3)(MASp)_n \rightarrow MAPbI_3 + 2MASp\uparrow \qquad (1)$$
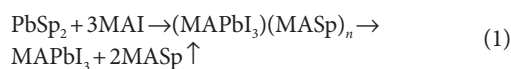
in which Sp^- denotes a spectator anion. The kinetics of the solid-state reactions are determined by the spectator anions in the precursors, with the reaction rate decreasing in the order of $NO_3^- > CH_3CO_2^- > Cl^- > I^-$ (REF. 87). Hydrohalic acids (HCl, HBr and HI) are also used as additives to produce smooth perovskite thin films without anti-solvent treatment[88–92]. A hydrohalic acid has two roles in tuning the growth kinetics: first, the acid provides excess anions to coordinate to Pb^{2+}, leading to the formation of an intermediate film after the solvent is removed[88], and second, the acid lowers the pH of the precursor solution and breaks down small clusters and nuclei, thus suppressing nucleation and crystal growth[93].

Lewis acid–base theory defines acceptors and donors of electron pairs as Lewis acids and bases, respectively[94]. Pb(II) halides are strong Lewis acids that readily form adducts with Lewis-basic solvents or additives. The formation of Lewis acid–base adducts in the precursor solution increases the solubility of lead halides and slows nucleation and crystal growth. By varying the basicity of the Lewis base and thus the strength of the interaction with the lead halide, the nucleation and crystal growth rates can be tuned. This approach can be used to improve the morphology of perovskite thin films. For example, the addition of DMSO or thiourea to a precursor solution of PbI_2 and MAI in DMF led to the formation of a Lewis acid–base adduct, and the morphology of the resultant thin film was greatly improved compared with the thin film obtained from the precursor solution without the Lewis-basic additive[95]. Other examples of Lewis-basic additives with the ability to modify perovskite thin-film morphologies are *N*-cyclohexyl-2-pyrrolidone[96], hexamethylphosphoramide (HMPA)[97], 1,8-diiodooctane[98] and thiosemicarbazide[99]. These additives have been demonstrated to improve the morphology of perovskite thin films, which would be beneficial for perovskite deposition over large-area substrates using various scalable deposition methods.

Surface modification of the substrates is another way to control the perovskite film morphology. Decreasing the surface energy of the substrate decreases the heterogeneous nucleation energy of the perovskite and promotes nucleation on the substrate surface, leading to films that are more compact. A thin layer of perylene was used to modify the surface of PEDOT:PSS (poly(3,4-ethylenedioxythiophene) polystyrene sulfonate) to improve the surface coverage of the resulting perovskite thin films[100]. Self-assembled monolayer (SAM) modification of the substrate surface improves wetting of the precursors on the substrates and thus improves the uniformity of the resulting perovskite thin films[101,102]. In another example, a surfactant, such as poly(vinylpyrrolidone), was added to the perovskite precursors to improve the surface coverage and smoothness of $MAPbI_{3-x}Cl_x$ thin films[103]. By contrast, non-wetting substrates were found to increase the perovskite grain size owing to larger spacing between the nuclei and easier grain-boundary migration associated with suppressed heterogeneous nucleation and a lower surface dragging force from the non-wetting substrates[104].

Two-step versus one-step deposition

Perovskite thin films have also been deposited through a two-step deposition route in which a lead halide thin film is first deposited and then converted to the perovskite by reaction with organic halide salts[105]. In comparison with the direct coating of a perovskite (for example, $MAPbI_3$) precursor, two-step deposition can be used to fabricate more compact films over larger areas; it is generally easier to deposit uniform PbI_2 thin films than perovskite thin films over a large area, and in the second step, the volume expansion that accompanies the conversion of PbI_2 to the perovskite fills any pinholes in the thin films. This advantage could alleviate the complications of morphology control in one-step deposition, especially with scalable deposition processes. The two-step approach has been widely used in the slot-die[106], electrodeposition[41,44] and spray coating[107–110] of perovskites. Large-area (~1 cm^2) PSCs with 13.1% efficiency have been fabricated by two-step spray deposition[107]. Another advantage of two-step deposition is the increased processing tolerance to a humid environment. Efficient PSCs can be fabricated in humid conditions using two-step methods[111,112]. The results indicate that small amounts of water in the organic halide solution can assist grain growth in perovskite thin films[113].

One disadvantage of the two-step deposition method is the long and variable reaction time required to convert the lead halide into the perovskite. In early work with two-step deposition, the lead halide films were usually soaked in an organic halide solution for >10 min, and mesoporous scaffolds were required to facilitate organic halide penetration for faster reaction between the lead halide and the organic halide salt[105]. Two-step reactions on planar devices either result in incomplete reaction or require longer reaction times. The long reaction time and indispensability of the mesoporous layer have limited our ability to scale two-step deposition. However, the addition of Lewis-basic additives can increase the rate of reaction between the lead halide film and the organic halide. For example, adduct formation between PbI_2 and DMSO increased the reaction rate of PbI_2 with FAI through an intramolecular exchange mechanism: DMSO in the PbI_2–DMSO complex readily exchanges with FAI, enabling the fast incorporation of FAI and thus rapid conversion to the perovskite[114]. This approach was used to fabricate PSCs with a record certified PCE of 22.1% and a 1 cm[2] device with a PCE of 19.7%[3]. Use of a Lewis base (for example, *N*-methyl-2-pyrrolidone (NMP)[115,116], HMPA[117], pyridine[118] or tributylphosphate[119]) has also been shown to promote rapid and complete conversion of PbI_2 to the perovskite. Adding MAI to PbI_2 precursors pre-expands the volume of PbI_2 and suppresses the subsequent volume expansion from PbI_2 to the perovskite while also facilitating the PbI_2–perovskite conversion[120]. All these strategies reduce the PbI_2–perovskite reaction barrier and shorten the reaction time in two-step deposition, which may be useful in scaling two-step deposition for PSCs.

Expanding processing windows

It is necessary to control the precursor processing window (that is, the time required for the wet precursor film to dry to form a solid-state film) of perovskite deposition to ensure reproducible and scalable PSC fabrication. When anti-solvent extraction is used to control the morphology of perovskite thin films, there is a strict time window in which compact perovskite films can be attained by applying the anti-solvent. It is therefore crucial to match the time window of anti-solvent application to the precursor processing window. Otherwise, the solvent will evaporate during deposition over large-area substrates, and the opportunity for conducting anti-solvent extraction could easily be missed. One approach to extending the time taken for solvent evaporation is to use carefully selected mixtures of solvents. For example, a mixed solvent of GBL and DMSO takes longer to evaporate than DMF from perovskite precursor solutions, owing to the adduct formation between DMSO and PbI_2 (REF. 16) (FIG. 5a). An even wider time window was achieved using a mixture of NMP and DMF, with an exceptionally long evaporation time of up to ~8 min. The development of solvent mixtures with ultra-long evaporation times enables anti-solvent bathing after blade coating on a large-area substrate (up to 20 cm[2]). A small-area (0.12 cm[2] aperture) device with a stable PCE of 19.05% and a module (12.6 cm[2] aperture) of PSCs with a PCE of ~12% have been fabricated

with blade coating and anti-solvent bathing[11]. Several solvent properties need to be considered when designing new solution chemistry: the boiling point and vapour pressure determine the evaporation rate of the solution, and the viscosity and surface tension affect the spreading of the precursor solution on substrates, with lower values favouring better wetting.
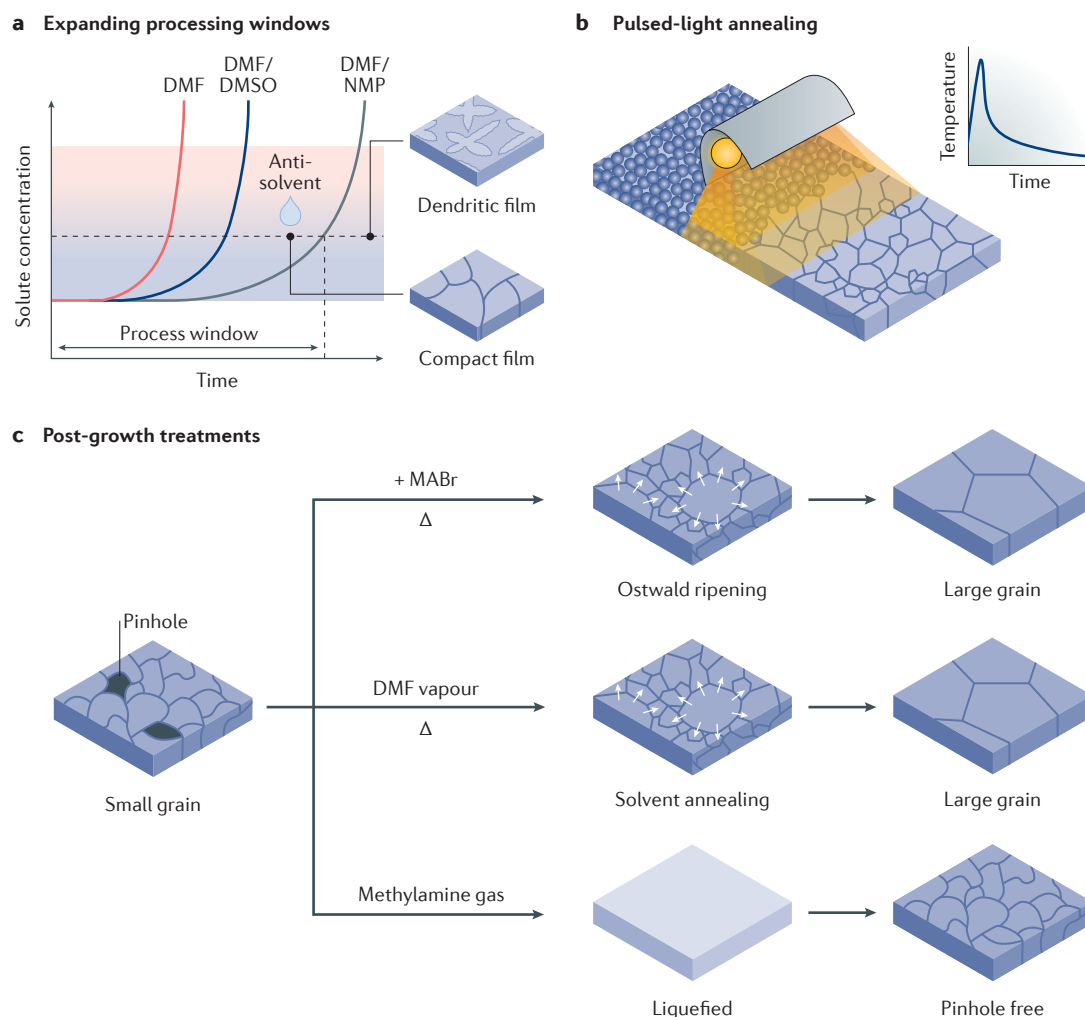
The annealing process

Thermal annealing is normally required after perovskite film deposition to increase crystallinity and grain size and to remove defects. These annealing steps are normally conducted using hot-plates and require prolonged processing times and extensive thermal energy. Annealing a perovskite layer usually takes 5–120 min. A long annealing time could negatively affect the production rate or make roll-to-roll fabrication lines impractically long. Adjusting the precursor chemistry (for example, using a MACl additive) has led to a substantial decrease in the required annealing times — from >10 min to <1 min (REF. 11).

Irradiation can be used to directly heat target materials, thereby reducing the processing time and the influence of heat on the underlying substrates. Therefore, irradiative heating is favourable for the roll-to-roll manufacturing of PSCs. Near-IR radiation was used to anneal a $MAPbI_{3-x}Cl_x$ perovskite absorber and reduced the processing time from 45 min to 2.5 s without a notable loss in PV performance[121]. The processing time was further reduced to only 1.5 ms using intensive photonic flash sintering generated by xenon flash bulbs. However, this initial demonstration of an ultrafast process resulted in non-uniform films and lower PV performance[122]. The current status of intense pulsed-light sintering or annealing (FIG. 5b) was examined in a recent review[123]. In another example, rapid thermal annealing by halogen lamp irradiation was used on $FAPbI_3$ perovskite layers. $FAPbI_3$ has better heat resistivity than $MAPbI_3$, which leads to better device reproducibility when treated with rapid thermal annealing. The optimal annealing time using the rapid thermal annealing approach was 40 s at 170 °C, a substantial decrease from the 10 min required using conventional hot-plates[124].

Post-growth treatment

Film uniformity and high surface coverage of perovskite thin films are crucial to the production yield of efficient perovskite modules. Even with myriad approaches of addressing morphology and uniformity issues, perovskite deposition is still fundamentally sensitive to the processing conditions. The variation of processing conditions over a large-area substrate typically results in decreased module performance owing to local pinholes and structural defects. Eliminating such defects is therefore a requisite for large-scale fabrication. Post-growth treatments (FIG. 5c) that improve the reproducibility of the process and increase the process tolerance may also be key to successfully scaling PSC fabrication.

An Ostwald ripening effect to heal structural defects in perovskite thin films has been demonstrated. $MAPbI_3$ films were treated with a dilute MABr solution

a Expanding processing windows

b Pulsed-light annealing

c Post-growth treatments

Figure 5 | **Expanding processing windows, pulsed-light annealing and post-growth treatments for the fabrication of perovskite thin films. a** | Expanding the precursor processing window is necessary for scaling up perovskite absorber layer deposition. The processing window is the time period in which compact perovskite films can be attained by applying the anti-solvent. Dendritic structures start to form after the processing window. Processing windows can be increased by using solvent mixtures that are slower to evaporate. **b** | Illustration of the irradiative annealing of perovskite thin films. Pulsed-light irradiation can be used to thermally anneal perovskite films and has led to a substantial decrease in the processing time relative to conventional heating approaches, such as the use of an oven or hot-plate. Thermal annealing can increase the crystallinity, increase the grain size and remove defects from perovskite thin films[123]. **c** | Schematics illustrating representative post-growth treatments for perovskite thin films: Ostwald ripening, solvent annealing and the addition of methylamine gas. DMF, *N,N*-dimethylformamide; DMSO, dimethyl sulfoxide; NMP, *N*-methyl-2-pyrrolidone. Panel **b** is adapted with permission from REF. 123, Elsevier.

($\sim 2\,mg\,ml^{-1}$), followed by brief annealing at 150 °C (REF. 125). The ripening process removed pinholes and increased the grain size and crystallinity of the perovskite thin film. Coalescence of small grains into larger grains can also be induced by annealing perovskite films in the vapour of polar solvents or organic halides. A reported DMF vapour annealing method increased the grain size and improved the electronic properties and PV performance of perovskite thin films[126]. Other polar solvents (for example, water, alcohols and DMSO) have been used for solvent annealing[127–129]. MAI vapour was also found to similarly induce grain growth in $MAPbI_3$ films[130].

A methylamine gas treatment approach can also be used to heal morphological defects in $MAPbI_3$ thin films[74]. Methylamine interacts with the perovskite and forms a liquid-state $MAPbI_3$–CH_3NH_2 intermediate phase that spreads smoothly on substrates. The methylamine gas treatment method can transform a poor-quality $MAPbI_3$ thin film with pinholes and dendritic structures into a smooth and compact thin film. Moreover, it can improve the device reproducibility of PSCs and increase the tolerance of the process to poor initial film morphology[131]. The microscopic structure of perovskite thin films can also be transformed with a pyridine (Py) gas treatment. Pyridine interacts reversibly with PbI_2 by forming a $PbI_2 \cdot x$Py Lewis acid–base adduct, and the pyridine vapour recrystallizes the thin film when it is inserted and subsequently extracted from the perovskite lattice[132].

Scaling up the charge-transport layers

Scalable deposition of the charge-transport layers (ETL and HTL) and the back electrode are also crucial to scaling up PSCs. The charge-transport layers should have appropriate interfacial energy alignment for charge transfer with the specific perovskite material and a suitable thickness and conductivity. Both inorganic and organic charge-transport materials have been used in PSCs. Common ETL materials in n–i–p PSCs include TiO_2, SnO_2 and ZnO, as well as some doped oxides[133–135]. HTL materials in n–i–p PSCs are more diverse and include organic small molecules (for example, spiro-OMeTAD (2,2′,7,7′-tetrakis(N,N-di-p-methoxyphenylamine)-9,9′-spirobifluorene))[136], polymers (for example, poly(triarylamine) (PTAA) and poly(3-hexylthiophene) (P3HT))[137] and inorganic materials (for example, CuI and CuSCN)[138,139]. The ETL in p–i–n PSCs is usually composed of fullerene or one of its derivatives (for example, [6,6]-phenyl-C_{61}-butyric acid methyl ester (PCBM) or indene–C_{60} bisadduct (ICBA))[140,141]. HTL materials for p–i–n PSCs include polymers (for example, PEDOT:PSS and PTAA)[104,140] and inorganic materials (for example, NiO_x and CuSCN)[142,143]. Large-area PSCs require a compact, uniform and pinhole-free charge-transport layer. Thermal stability, process complexity and energy and time consumption, which add to cost, are also important considerations for scaling. Many charge-transport materials in PSCs originate from the fields of DSSCs and OPVs. Thus, scalable deposition of these layers can benefit from knowledge gained in fabricating DSSC and OPV modules.

Electron-transport layer

The most common ETL in n–i–p PSCs is TiO_2. A compact TiO_2 layer can be deposited by either spray pyrolysis or a sol–gel method on glass substrates. Vacuum-based processes, such as radio-frequency sputtering[144], thermal oxidation of a sputtered titanium film[145] and electron-beam evaporation[146], are also used to generate uniform and high-quality compact TiO_2 films over large areas, but these processes usually require high-temperature annealing, which is often undesirable for flexible polymer substrates. Compact TiO_2 layers have also been deposited by low-temperature techniques, including atomic layer deposition[147,148], $TiCl_4$ chemical bath deposition[149], hydrothermal reaction[150] and electrodeposition[151]. For example, a compact TiO_2 layer was deposited on an indium-doped tin oxide (ITO)-coated polyethylene terephthalate (PET) film using atomic layer deposition. UV irradiation was also used to selectively sinter a TiO_2 mesoporous scaffold without affecting the polymer substrate underneath. This selective irradiation sintering enabled the fabrication of PSC modules on flexible PET substrates of up to 30 cm² (REF. 148).

SnO_2 is another representative ETL material used for PSCs, and there are several reasons for replacing TiO_2 with SnO_2 in PSCs: SnO_2 has a higher open-circuit voltage (V_{OC}), smaller J–V hysteresis and negligible photocatalytic effect, which is beneficial for the long-term stability of PSCs[134,152,153]. Despite these advantages, deploying SnO_2 in PSCs on a large scale is challenging. The optimized thickness of the SnO_2 layer in PSCs is thinner than that of TiO_2; thus, it is more challenging to obtain a pinhole-free layer, especially on rough fluorine-doped tin oxide (FTO) substrates. When SnO_2 is processed at high temperatures, it is usually too crystalline and conductive, and therefore cannot be used as an effective ETL in PSCs. Thus, SnO_2 films are normally deposited with low-temperature sol–gel deposition, atomic layer deposition, chemical bath deposition, hydrothermal reaction, colloidal solution approach and electrodeposition processes[134,152–155].

Hole-transport layer

PEDOT:PSS is widely used as the HTL in inverted PSCs. However, PEDOT is hygroscopic and absorbs water from the environment, which is detrimental to the stability of the PSC[156]. NiO_x is a popular alternative to PEDOT, and it can be deposited using scalable deposition techniques such as sol–gel, spray pyrolysis, atomic layer deposition, sputtering and electrodeposition[142,157–161]. NiO_x-based HTLs are usually annealed at 300–500 °C to increase their crystallinity and conductivity. The high-temperature treatment hinders the use of NiO_x-based HTLs on flexible substrates. To address this challenge, a room-temperature solution processing method was developed to deposit pre-synthesized NiO_x nanocrystals to form a high-quality compact layer, leading to flexible PSCs with a PCE of 14.5%[162]. In a similar two-step approach, NiO_x nanocrystals were prepared using the flame-spray method, which enables high-throughput synthesis (~1 kg h⁻¹) and requires no additional annealing step to form highly crystalline NiO_x nanocrystals[163]. CuSCN is also widely used as the HTL in PSCs and can be deposited by blade coating, spray coating and electrodeposition[139,143,164]. All these materials have the potential to be used in the scalable fabrication of perovskite modules.

The perovskite absorber layer, ETL and HTL of a PSC can be deposited using scalable deposition methods, but most scaling studies have focused on the scalable deposition of just one or two of the functional layers. Only a few studies have demonstrated fully printable PSCs. In one example, only blade coating was used to fabricate PSCs with a structure of PEDOT:PSS/$MAPbI_{3−x}Cl_x$/PCBM/bis-C_{60}/Ag. With this device structure, the PCE of a blade-coated PSC is comparable to the PCE of a spin-coated PSC (10.4% and 11.0%, respectively)[83]. In another example of a fully slot-die printed PSC, the molecular structure of the HTL was designed to improve the morphology of the printed HTL film. Bifluo-OMeTAD (2,2′,7,7′-tetrakis(N,N-di-p-methoxyphenyl)amine-9,9′-bifluorenylidene) is an analogue of the common HTL spiro-OMeTAD; bifluo-OMeTAD was designed to have a fully π-conjugated structure and exhibits less crystalline aggregation, a smoother film morphology and higher substrate coverage than spiro-OMeTAD. With the bifluo-OMeTAD HTL, PSCs fabricated solely by slot-die coating exhibited a PCE of 14.7%, which is higher than their spiro-OMeTAD counterparts[165]. Although some progress has been made, more effort is clearly required to develop fully scalable deposition schemes for all device layers so that PSCs can make the transition from the laboratory to a deployable technology.

Scalable deposition of the back electrode

Back electrodes for PSCs are mostly deposited by thermal evaporation. Evaporation is a scalable process and has been used for producing aluminium-coated packaging foils. Sputtering has been less explored for electrode deposition in PSCs, although the process is more favourable for large-scale fabrication as it is less dependent on the vacuum level and generally has shorter processing times than evaporation. The greatest challenge is ion bombardment damage of the organic charge-transport layer, which can be mitigated by inserting an inorganic buffer layer (for example, ZnO or MoO_x)[166,167]. Sputtering can be used to deposit metallic films, alloys or more complex compounds, such as transparent conducting oxides (for example, ITO or aluminium-doped zinc oxide (AZO)), which are common in semi-transparent devices and tandem applications. Oxide-based back electrodes also provide stability benefits to PSCs, which are discussed in the following section.

Vacuum-free processes for depositing back contacts are highly desirable to fully exploit the solution processing advantages of PSCs. The use of screen-printed silver electrodes in slot-die-coated PSCs yielded only a slightly lower PCE than cells with silver electrodes fabricated through evaporation (6.4% versus 7.9%, respectively), showing the potential of vacuum-free fabrication[84]. Silver nanowire networks (suitable for semi-transparent PSCs) can be deposited by spray coating[168]. Another example of vacuum-free deposition is the development of a flexible adhesive electrode consisting of a nickel mesh and a layer of a conductive PEDOT:PSS/acrylic adhesive[169]. The flexible electrode can be laminated and bonded to the solar cell with a conductive adhesive to transport charges. The lamination process does not affect the underlying perovskite or HTL layers, and this process can be deployed in roll-to-roll fabrication[169].

Carbon is also an excellent candidate material for PSC electrodes because it is abundant, inexpensive, chemically stable and environmentally benign. Different forms of carbon materials, including graphite, carbon soot, carbon nanotubes and graphene, have been demonstrated as back electrodes in PSCs[22,23,170,171]. One outstanding example is an architecture composed of mesoporous-TiO_2/ZrO_2/perovskite/carbon (carbon black and graphite), for which all the layers can be screen printed, thus making the device fully scalable[22]. A perovskite module with a carbon electrode has been fabricated on a $10\,cm \times 10\,cm$ substrate with an active-area efficiency of more than 10% and with a GFF of ~50%[172,173]. Subsequently, the GFF was further improved to above 60%, leading to a certified module PCE of 9.1%[174].

PSC and module stability

Stability and reliability at the module level are crucial for ensuring the commercial success of perovskite PV technology. There has been substantial progress in improving the PSC stability at the cell level over the past few years (FIG. 6a) owing to continuous research effort and a better understanding of the degradation mechanisms. This topic has been thoroughly reviewed in several recent articles, in which more detailed information can be found[175–178]. In general, better PSC stability can be achieved with improvement across the device components by modifying the perovskite composition and the choice of charge-transport layers and electrode material. Recent demonstrations have shown the importance of the interfaces within the device. Further understanding of how the interfaces change over time along with associated degradation processes is needed to realize perovskite modules that have no stability issues[179].

Perovskite composition

$MAPbI_3$ is prone to decomposing into PbI_2, CH_3NH_2 and HI upon exposure to heat or moisture[180]. $FAPbI_3$ has better resistance to heat and moisture, but pure $FAPbI_3$ is not stable in the cubic structure and tends to transform into a hexagonal structure and become non-photoactive. Alloying FA^+ with smaller cations (for example, MA^+, Cs^+ or Rb^+) can stabilize the perovskite structure and suppress phase transition[181–183] (FIG. 6b). Partially replacing I^- with Br^- (<15 mol%) has also been shown to improve stability[184]. A PSC with a FA-based mixed-cation (RbCsMAFA) perovskite showed impressive stability against heat and light soaking, retaining 95% of the initial PCE after ageing for 500 h at 85 °C with continuous illumination (AM1.5, one sun equivalent from a white light-emitting diode) under N_2 atmosphere[183]. Long-chain or bulky organic ammonium cations can passivate the perovskite surfaces and block moisture ingression[185,186]. A 2D–3D perovskite composed of both MA^+ and butylammonium (BA^+) also exhibited a strong resistance against moisture-induced degradation, maintaining 70% of the initial PCE after 2,000 h of one-sun illumination under ambient conditions[187].

Charge-transport layers

The stability of charge-transport layers and their interfaces with perovskite materials are crucial to the stability of PSCs[179]. The conventional ETL, TiO_2, has a photocatalytic effect and can cause perovskite degradation under UV illumination. Better stability can be attained with alternative ETLs, such as SnO_2, $BaSnO_3$ and chloride-treated TiO_2 nanoparticles[188–190]. Spiro-OMeTAD, the most commonly used HTL, can also introduce a stability issue in PSCs. Spiro-OMeTAD HTL films often have pinholes, which facilitates moisture ingression and leads to attack of the perovskite layer[165,191]. Lithium bis(trifluoromethane)sulfonimide (LiTFSI) is often used as a dopant in spiro-OMeTAD to increase its conductivity. However, the hygroscopic LiTFSI dopant in spiro-OMeTAD films attracts water, and the Li^+ ions are highly mobile and can migrate into the perovskite layer and potentially accelerate device degradation[192]. HTLs based on hydrophobic molecules and dopants have delivered improved stability[193]. Dopant-free polymer HTLs are also promising for the fabrication of stable PSCs[194,195]. Other potential HTLs for PSCs with long-term stability are inorganic HTLs, such as carbon nanotubes, NiO_x, CuI and CuSCN, which are generally denser than their organic counterparts[138,196–198]. In one example, CuSCN was used as the HTL in a PSC, and the device achieved a lifetime of more than 1,000 h (retaining >95% of the initial PCE) under full-sun illumination at 85 °C (REF. 198).
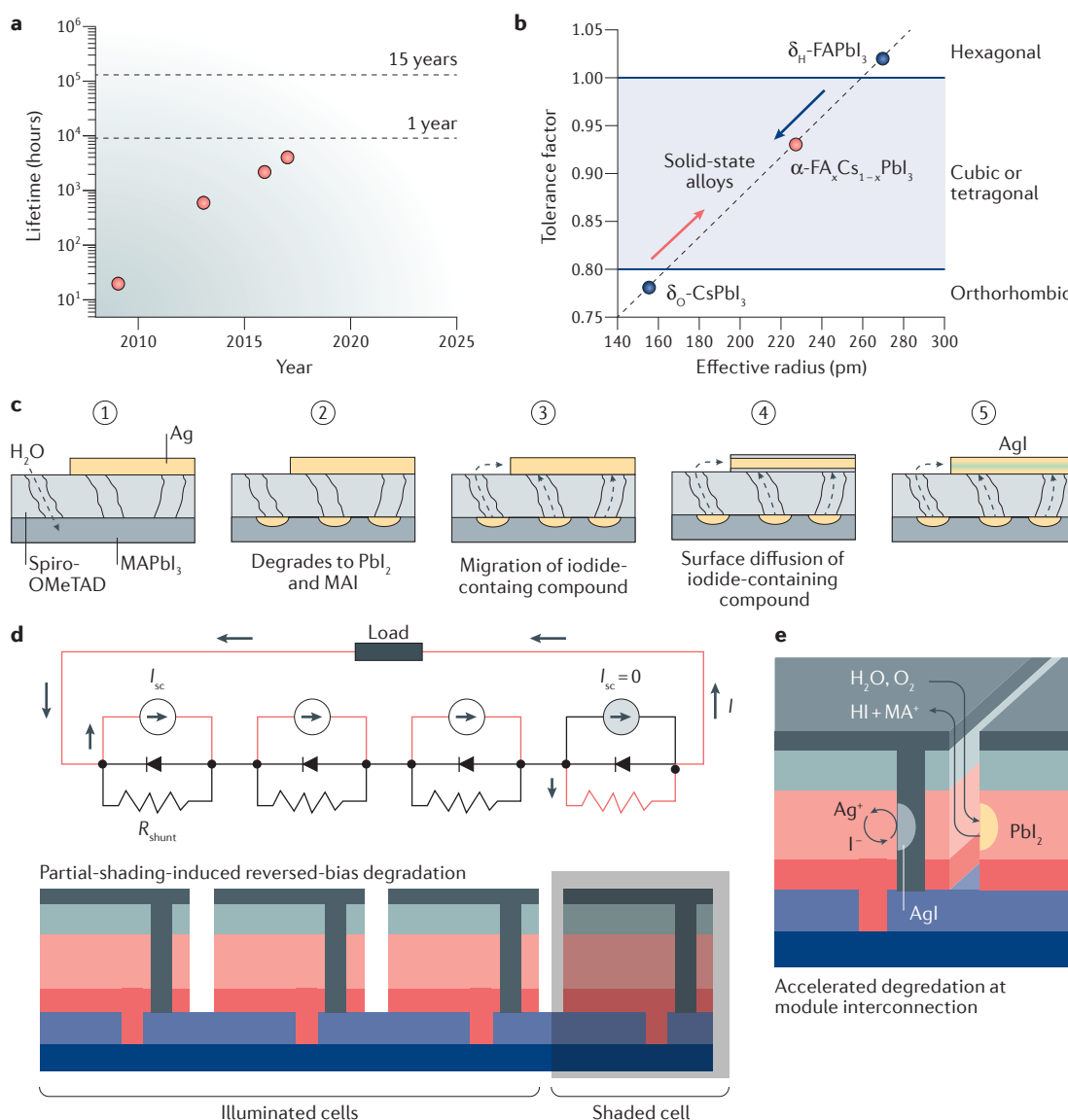
Figure 6 | **Stability of perovskite solar cells and modules. a** | Over the past decade, there has been a rapid increase in the stability of perovskite solar cells (PSCs)[178]. The average lifetime of a PSC has increased from hours in 2009 to about a year in 2017. **b** | The cubic structure of the formamidinium lead iodide (FAPbI$_3$) perovskite is not stable and undergoes a phase transition to the non-photoactive hexagonal structure. The cubic structure of FAPbI$_3$ can be stabilized through tuning the perovskite structure tolerance factor (an empirical parameter used to predict stable perovskite crystal structures) by adjusting the effective radius of the A-site cation[182]. **c** | Schematics showing the degradation process of the back contact caused by AgI formation[199]. Moisture ingresses through pinholes in the spiro-OMeTAD (2,2',7,7'-tetrakis (N,N-di-p-methoxyphenylamine)-9,9'-spirobifluorene) layer and causes decomposition of the perovskite to PbI$_2$ and methylammonium iodide (MAI). The iodide-containing compounds released through perovskite decomposition react with the Ag electrode and form AgI. **d,e** | Module-related reliability issues in perovskite solar modules. Partial shading of the module causes reverse bias and shunting failure in the shaded cells. Iodide from the perovskite layer can rapidly erode metal electrodes at interconnections. The openings between individual cells are exposed to ambient air and subjected to fast decomposition caused by moisture and oxygen. *I*, current; I_{sc}, short-circuit current; MA$^+$, methylammonium; R_{shunt}, shunt resistance. Panel **a** is adapted from REF. 178, Macmillan Publishers Limited. Panel **b** is adapted with permission from REF. 182, American Chemical Society. Panel **c** is adapted with permission from REF. 199, Wiley-VCH.

Electrode materials

Although the electrode materials are not in direct contact with the perovskite layer, the stability of the electrode materials is also important to the long-term operation of PSCs. Silver electrodes react with halides to form silver halides[199] (FIG. 6c). Gold electrodes are more stable, but it has been shown that gold can diffuse into the perovskite layer and cause irreversible device degradation[200]. The degradation of the electrode materials could be more serious at the module scale than in a single cell, as the electrode material at the interconnection region is in direct contact with the perovskite, which can

lead to faster corrosion. Metal oxides have better resistance against halide corrosion, and they can be used as barriers to protect the metal electrodes. Double-layer electrodes, such as Cr_2O_3/Cr, MoO_x/Al and ZnO/Al, have shown improved stability in PSCs[156,201,202]. TCOs can also serve as back electrodes in PSCs. For example, ITO was shown to be more stable than metal electrodes in PSCs, with ITO both eliminating electrode corrosion and alleviating perovskite egression. Even with thermally unstable $MAPbI_3$, devices with ITO electrodes yielded a T_{80} lifetime (the time taken to reach 80% of the initial efficiency) of 120 h at 100 °C, whereas cells based on metal electrodes failed within minutes[167]. PSCs with a porous carbon back electrode usually exhibit exceptional long-term stability (>1,000 h) under light and ambient conditions; the thick carbon electrode can effectively encapsulate the device, preventing external moisture ingress and internal perovskite egress[39]. A PSC with a carbon electrode, a glass seal and a UV-filter yielded a lifetime of 10,000 h at 55 °C (REF. 172).

Encapsulation
In addition to continuously improving the stability of PSCs through advances in material properties, encapsulation can serve as extra protection against degradation. Encapsulation with, for example, a fluoropolymer, hydrophobic carbon electrode and/or metal oxide barrier layer has been used to improve the stability of PSCs to levels similar to those reported for devices operating under N_2 or another inert atmosphere[39,156,197,203]. In another example, $FA_{1-y}Cs_yPb(I_{1-x}Br_x)_3$ PSCs were encapsulated by two glass sheets, and the edges were sealed with commercial sealants (ethylene vinyl acetate and butyl rubber). These PSCs passed stability tests under the International Electrotechnical Commission's damp–heat conditions (85 °C and 85% relative humidity for 1,000 h), validating other cell-level tests and demonstrating the promise of stabilizing PSCs using the encapsulation strategy[177]. Future research directions will include exploring low-cost and reliable encapsulation materials as well as developing processes to minimize the impact on modules during encapsulation.

Module-related degradation
Degradation at the module level is more complicated than at the single-cell level. In addition to the potential of additional processing-induced degradation pathways in the more complex production of modules, certain reliability concerns are unique to monolithically interconnected PSC modules, such as the halogen-induced degradation of module interconnections, degradation or module failure caused by partial shading and material fatigue and/or structure failure owing to ion migration. In a partially shaded module, the shaded cells are subjected to a high reverse bias, which could lead to local hot spots and inverted-bias junction damage[204,205] (FIG. 6d,e). These same effects might also couple to intrinsic and extrinsic ionic conduction phenomena to change the module performance over time. Thus, it is necessary to investigate the stability of PSCs under reverse bias and in realistic module configurations.

Characterization of modules
When transitioning from laboratory-scale to module-level development, it is important to be able to evaluate and control the uniformity of the material properties at the film and device levels, the distribution of defects related to the material, device and operation, and the locations of shorts and shunts, as well as the interconnection properties in modules. Techniques suitable for characterizing and guiding the development of large-area perovskite thin-film solar cells and modules are discussed below.

Composition, structure and properties
Characterization of the composition, structure and properties of perovskites is important for developing PSC fabrication technology. The most common characterization techniques for small-area PSCs are X-ray diffraction (XRD), UV–vis spectrophotometry, scanning electron microscopy (SEM), optical microscopy, photoluminescence (PL) and X-ray photoelectron spectroscopy/UV photoelectron spectroscopy (XPS/UPS). These characterization techniques coupled with a mapping capability can be used to study the uniformity and homogeneity of perovskite thin films for large-area device and/or module development. High-speed inline optical imaging, UV–vis and X-ray fluorescence (XRF) spectroscopy (FIG. 7a) inspection technologies will be helpful for industrial fabrication, and they have been widely used for quality control in traditional PV fabrication. For example, an in situ X-ray scattering system was developed for a roll-to-roll perovskite coater. The system was used to study the formation and degradation of perovskites on flexible substrates, but it can also be used to investigate the crystalline uniformity of roll-to-roll-coated films[206].

Cell performance and current mapping
$J–V$ curves and incident photon-to-current efficiency (IPCE) are mostly used to evaluate the performance of small-area devices. However, $J–V$ and IPCE tests with spot-size illumination or a small-area electrode have been used to characterize the uniformity of large-area perovskite devices[59,62,83]. Light-beam-induced current (LBIC) mapping uses a small laser spot to scan the active area of solar cells and provides a local photocurrent generation profile of the device. LBIC mapping has been used to map an 8 cm² perovskite solar module; the inhomogeneous current distribution clearly revealed the non-uniformity of the perovskite films, thus indicating the need to improve the coating uniformity in future device optimization[207]. LBIC mapping is also used to investigate the degradation mechanism of PSCs under different ambient conditions[208] (FIG. 7b).

Photoemission spectroscopy and imaging
Solar cells are optimized for light harvesting and subsequent carrier separation. Reversing the process, that is, applying a forward bias and injecting carriers into the device, leads to carrier recombination and photon emission. Electroluminescence (EL) is the basic working mechanism of semiconductor light-emitting diodes,
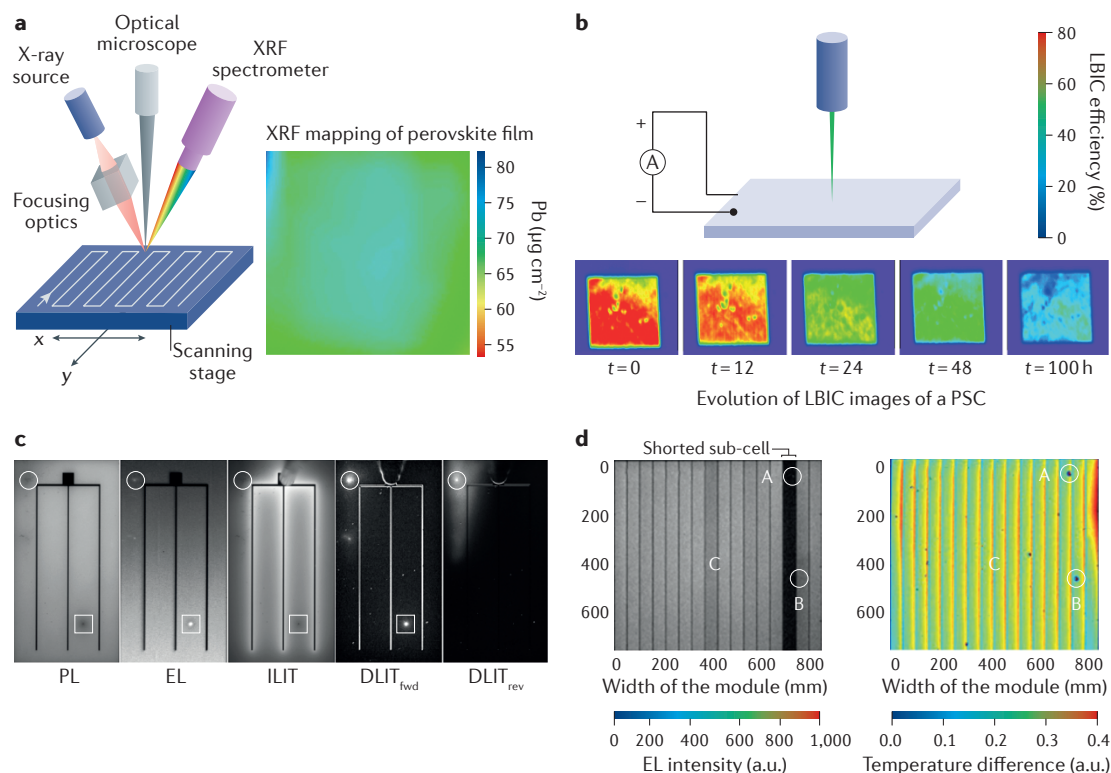
Figure 7 | Typical characterization techniques suitable for large-area solar cells and modules. a | X-ray fluorescence (XRF) can be used for elemental mapping (for example, lead) of large-area perovskite thin films[11]. **b** | Light-beam-induced current (LBIC) mapping of perovskite solar cells (PSCs) showing non-homogeneous current generation in the PSCs and the evolution of PSC degradation under 80% relative humidity[208]. **c** | Photoluminescence (PL), electroluminescence (EL) and lock-in thermography (LIT) images of a copper indium gallium selenide (CIGS) solar cell; the circles highlight a shunting defect, and the squares indicate a local recombination centre or weak diode region[216]. **d** | EL (bias current (J_{bias}) = 2.5 mA cm^{-2}) and LIT (J_{bias} = 25 mA cm^{-2}) images of an amorphous silicon module; one of the sub-cells (appearing darker in the EL image) is shorted by a defect in the interconnection, as shown by point A in the LIT image. Point C is a non-detrimental defect that results in a slightly darker cell in the EL image, and point B is caused by an IR-camera defect[217]. DLIT, dark lock-in thermography; ILIT, illuminated lock-in thermography. Panel **a** (right) is reproduced from REF. 11, Macmillan Publishers Limited. Panel **b** is reproduced with permission from Song, Z. et al. Investigation of degradation mechanisms of perovskite-based photovoltaic devices using laser beam induced current mapping, Proc. SPIE **9561**, 956107 (2015), REF. 208. Panel **c** is reprinted with permission from Johnston, S. et al. Correlations of Cu(In, Ga)Se$_2$ imaging with device performance, defects, and microstructural properties. *J. Vac. Sci. Technol. A* **30**, 04111D (2012). Copyright 2012, American Vacuum Society, REF. 216. Panel **d** is reproduced with permission from REF. 217, Elsevier.

and it can be used to study non-radiative recombination in PSCs and to predict the theoretical V_{OC} limits of devices[209,210]. An EL imaging setup for a PSC is relatively simple because perovskites have a larger bandgap than silicon (the most common material used in charge-coupled device arrays), and the data acquisition speed in EL imaging is much faster than in LBIC mapping. An EL image can provide information about charge recombination at the nanoscale[211] and macroscopic charge-transport obstacles associated with non-uniformity, impurities, shunting and internal resistance[70,212–215]. EL and PL are usually used as complementary methods to reveal macroscopic defects in devices (FIG. 6c). Recombination centres, weak diodes and shunting regions suppress the radiative recombination of carriers; thus, they appear darker in the EL and PL images. Regions with higher contact resistance impede current injection and photon-generated carrier dissipation, resulting in weaker EL and stronger PL features in the images[175,178].

Lock-in thermography

Lock-in thermography (LIT) is also a useful imaging tool for identifying local defects in solar cells (FIG. 7c). LIT can be operated in three modes, with each mode being sensitive to different types of defects. Illuminated LIT (ILIT) generates a photovoltage in solar cells with pulse illumination. When charge carriers recombine at the locations of recombination centres, weak diodes or shunting paths, heat is generated, which can be detected by an IR camera. Dark LIT (DLIT) can be operated at forward or reverse bias: DLIT$_{fwd}$ detects heat at shunted spots, weak diode locations or regions with poor contact and high series resistance, whereas DLIT$_{rev}$ is sensitive to shunts that conduct current at reverse bias[216].

Interconnections in modules

In addition to the film and device uniformity, the interconnections are another key determinant of module operation. LIT in conjunction with EL and PL imaging

is useful for identifying the shunting, shorts and high-resistance regions in individual sub-cells and inter-connections in solar modules. In general, a shunted or shorted sub-cell appears darker in an EL image because the current passes through shunting points instead of the absorber layer. In this situation, a local hot spot appears at the shunting point owing to Joule heating, resulting in a brighter spot in the DLIT image. High sheet resistance or series resistance is also recognizable from DLIT images under high forward-injection conditions. FIGURE 7d shows EL and LIT images of an amorphous silicon thin-film solar module with one shorted sub-cell. The shorting location in the interconnection can be seen as a hot spot in the LIT image[217].

Module cost and life cycle assessment

There are two main challenges for large-scale PV technologies: first, enabling the low-cost production of PV systems at scale and second, achieving sustainability (including ensuring resource availability and minimizing any negative environmental impact) in the case of terawatt-scale deployment[14]. Insight regarding the former has been gained through several cost model studies based on hypothesized device stacks and production workflows[218–220]. These studies show clear cost advantages of PSCs over other PV technologies. However, the various attempts to examine the cost competitiveness of PSCs must be viewed critically, because some of the device-stack configurations examined may not be feasible to implement at scale in the future. This points to a range of opportunities for innovations in device-stack configurations and/or materials for large-scale PSCs but also highlights the difficulty in undertaking realistic cost assessments of deployable PSCs at this nascent stage of technology development and with the present lack of certainty regarding module requirements (for example, encapsulation, weight and structure). Although there has been continued progress, the factor that remains most uncertain is the stability[218].

Life cycle assessments provide insight into the environmental impact and the sustainability of a particular PSC stack. Life cycle assessments rely on more well-established energy and CO_2 costs associated with materials production rather than direct monetary costs. The life cycle assessments of PSCs to date have looked at only a few (of the many) PSC architectures. In one study, an energy payback time of less than 0.3 years for PSCs with an n–i–p structure was calculated, which is much shorter than that of other PV technologies[221]. It is important to note the limited extent to which life cycle assessments have so far been used in comparing PSCs with other established technologies. In the context of terawatt-scale energy production and the development of a sustainable PV economy, the cost of production as well as the cost of refurbishing and/or disposing of any PV must also be considered.

Challenges and outlook

Although PSCs have already shown promise towards large-scale deployment, many challenges remain. Key materials and processing challenges include the fully scalable fabrication of all device layers and reliable schemes for module interconnection. These challenges are further complicated because the most ideal device architecture has not yet been identified; several architecture–materials combinations have shown high performance, with good progress in terms of stability at the cell level. In addition, the composition of perovskites has become increasingly complex for high efficiency and/or stability in laboratory-scale devices. Transferring the new material compositions to production scale requires more effort in process engineering because of changes in the material processing properties. Lowering the cost and environmental impact of the final PV modules will require further reductions in the cost and energy consumption of resource extraction, material synthesis and film processing for the different components in PSCs — especially for the noble metal electrode (gold), transparent conducting substrates (ITO or FTO), spiro-OMeTAD-based HTL and fullerene-based ETL. Some alternative materials with great potential have been proposed and demonstrated, such as double-layer MoO_x/Al and Cr_2O_3/Cr back electrodes[201,222]. As perovskite technology matures, the ideal device architecture, with scalable materials, and module fabrication process will likely be identified. This will enable more reliable

Table 2 | Examples of companies and research organizations with industrial partners working on the scale up of PSCs

Company or organization	Country or region	Progress in scale up or technology interest	Date of news release
Greatcell Solar (formerly Dyesol)	Australia	Demonstrated a 20 cm² perovskite module	23 Nov 2015
Microquanta Semiconductor	China	Demonstrated a 16 cm² module with a certified PCE of 16.0%	23 May 2017
Oxford Photovoltaics	United Kingdom	Developing perovskite/silicon tandem solar cells	–
Saule Technologies	Poland	Developing inkjet-printed flexible PSCs	–
Solaronix	Switzerland	Demonstrated a 500 cm² module with a PCE of 12%	11 Jul 2016
Solliance Solar Research	Europe	Demonstrated a 16 cm² module with a certified aperture PCE of 12.4%	11 Apr 2017
		Demonstrated a 168 cm² module with an aperture PCE of 10%	09 May 2016
Toshiba	Japan	Demonstrated a 25 cm² module with a PCE of 10.5% on a flexible substrate	25 Sep 2017
Weihua Solar (acquired by Golden Concord)	China	Demonstrated a 25 cm² module with a PCE of 10.6% as well as a 45 cm × 65 cm module	–

PCE, power conversion efficiency; PSC, perovskite solar cell.

cost modelling and life cycle assessments of the suitability of perovskite PVs for terawatt-scale deployment.

Finally, on the basis of the remarkable progress in the efficiency and stability of PSCs, it is increasingly important to consider these performance metrics in the context of scalability. We are still at an early stage of understanding and addressing the challenges of scaling up PSCs with respect to the myriad device stacks and effective schemes for module interconnection. However, the rapid development towards scaling up at a relevant performance level (efficiency and stability) coupled with the low-cost manufacturing capability has already attracted substantial industrial interest worldwide (TABLE 2). The challenges for PSC scaling outline clear research needs that are informed by industry through the potential supply chain for PSCs to ensure that highly scalable choices are made at the same time that the efficiency and stability are improved. If these issues can be addressed, the potential for PSCs, compared with other PV technologies, to have an impact on global energy production at the terawatt scale is unrivalled.

1. Kojima, A., Teshima, K., Shirai, Y. & Miyasaka, T. Organometal halide perovskites as visible-light sensitizers for photovoltaic cells. *J. Am. Chem. Soc.* **131**, 6050–6051 (2009).
2. Kim, H.S. et al. Lead iodide perovskite sensitized all-solid-state submicron thin film mesoscopic solar cell with efficiency exceeding 9%. *Sci. Rep.* **2**, 591 (2012).
3. Yang, W. S. et al. Iodide management in formamidinium-lead-halide-based perovskite layers for efficient solar cells. *Science* **356**, 1376–1379 (2017).
4. National Revewable Energy Laboratory. NREL solar cell efficiency chart. *NREL* www.nrel.gov/pv/assets/images/efficiency-chart.png (2017).
5. Ndione, P. F., Li, Z. & Zhu, K. Effects of alloying on the optical properties of organic–inorganic lead halide perovskite thin films. *J. Mater. Chem. C* **4**, 7775–7782 (2016).
6. Steirer, K. X. et al. Defect tolerance in methylammonium lead triiodide perovskite. *ACS Energy Lett.* **1**, 360–366 (2016).
7. Yin, W.J., Shi, T. & Yan, Y. Unusual defect physics in CH₃NH₃PbI₃ perovskite solar cell absorber. *Appl. Phys. Lett.* **104**, 63903 (2014).
8. De Wolf, S. et al. Organometallic halide perovskites: sharp optical absorption edge and its relation to photovoltaic performance. *J. Phys. Chem. Lett.* **5**, 1035–1039 (2014).
9. Stranks, S. D. et al. Electron-hole diffusion lengths exceeding 1 micrometer in an organometal trihalide perovskite absorber. *Science* **342**, 341–344 (2013).
10. Xing, G. et al. Long-range balanced electron- and hole-transport lengths in organic-inorganic CH₃NH₃PbI₃. *Science* **342**, 344–347 (2013).
11. Yang, M. et al. Perovskite ink with wide processing window for scalable high-efficiency solar cells. *Nat. Energy* **2**, 17038 (2017).
   Report on the development of a slow-drying perovskite precursor to enable anti-solvent extraction in scalable deposition.
12. Tang, S. et al. Composition engineering in doctor-blading of perovskite solar cells. *Adv. Energy Mater.* **7**, 1700302 (2017).
13. Chen, H. et al. A solvent- and vacuum-free route to large-area perovskite films for efficient solar modules. *Nature* **550**, 92–95 (2017).
   Study demonstrating a route to an efficient large-area PSC module using methylamine gas-containing perovskite precursors.
14. Berry, J. J. et al. Perovskite photovoltaics: the path to a printable terawatt-scale technology. *ACS Energy Lett.* **2**, 2540–2544 (2017).
15. Green, M. A. et al. Solar cell efficiency tables (version 50). *Prog. Photovolt. Res. Appl.* **25**, 668–676 (2017).
16. Jeon, N. J. et al. Solvent engineering for high-performance inorganic–organic hybrid perovskite solar cells. *Nat. Mater.* **13**, 897–903 (2014).
   Report on the anti-solvent extraction method for control of the perovskite film morphology.
17. Wojciechowski, K. et al. Heterojunction modification for highly efficient organic–inorganic perovskite solar cells. *ACS Nano* **8**, 12701–12709 (2014).
18. Hou, Y. et al. Low-temperature and hysteresis-free electron-transporting layers for efficient, regular, and planar structure perovskite solar cells. *Adv. Energy Mater.* **5**, 1501056 (2015).
19. Ke, W. et al. Cooperative tin oxide fullerene electron selective layers for high-performance planar perovskite solar cells. *J. Mater. Chem. A* **4**, 14276–14283 (2016).
20. Yang, D. et al. Surface optimization to eliminate hysteresis for record efficiency planar perovskite solar cells. *Energy Environ. Sci.* **9**, 3071–3078 (2016).

21. Yoon, H., Kang, S. M., Lee, J.K. & Choi, M. Hysteresis-free low-temperature-processed planar perovskite solar cells with 19.1% efficiency. *Energy Environ. Sci.* **9**, 2262–2266 (2016).
22. Ku, Z., Rong, Y., Xu, M., Liu, T. & Han, H. Full printable processed mesoscopic CH₃NH₃PbI₃/TiO₂ heterojunction solar cells with carbon counter electrode. *Sci. Rep.* **3**, 3132 (2013).
23. Li, Z. et al. Laminated carbon nanotube networks for metal electrode-free efficient perovskite solar cells. *ACS Nano* **8**, 6797–6804 (2014).
24. Etgar, L. et al. Mesoscopic CH₃NH₃PbI₃/TiO₂ heterojunction solar cells. *J. Am. Chem. Soc.* **134**, 17396–17399 (2012).
25. Moon, S. J. et al. Laser-scribing patterning for the production of organometallic halide perovskite solar modules. *IEEE J. Photovolt.* **5**, 1087–1092 (2015).
26. Green, M. A., Emery, K., Hishikawa, Y., Warta, W. & Dunlop, E. D. Solar cell efficiency tables (version 39). *Prog. Photovolt. Res. Appl.* **20**, 12–20 (2012).
27. Seo, J. et al. Benefits of very thin PCBM and LiF layers for solution-processed p–i–n perovskite solar cells. *Energy Environ. Sci.* **7**, 2642–2646 (2014).
28. Huang, L. et al. Efficient and hysteresis-less pseudo-planar heterojunction perovskite solar cells fabricated by a facile and solution-saving one-step dip-coating method. *Org. Electron.* **40**, 13–23 (2017).
29. He, M. et al. Meniscus-assisted solution printing of large-grained perovskite films for high-efficiency solar cells. *Nat. Commun.* **8**, 16045 (2017).
30. Ye, F. et al. Soft-cover deposition of scaling-up uniform perovskite thin films for high cost-performance solar cells. *Energy Environ. Sci.* **9**, 2295–2301 (2016).
31. Chang, W.C., Lan, D.H., Lee, K.M., Wang, X.F. & Liu, C.L. Controlled deposition and performance optimization of perovskite solar cells using ultrasonic spray-coating of photoactive layers. *ChemSusChem* **10**, 1405–1412 (2017).
32. Das, S. et al. High-performance flexible perovskite solar cells by using a combination of ultrasonic spray-coating and low thermal budget photonic curing. *ACS Photon.* **2**, 680–686 (2015).
33. Liang, Z. et al. A large grain size perovskite thin film with a dense structure for planar heterojunction solar cells via spray deposition under ambient conditions. *RSC Adv.* **5**, 60562–60569 (2015).
34. Heo, J. H., Lee, M. H., Jang, M. H. & Im, S. H. Highly efficient CH₃NH₃PbI₃₋ₓClₓ mixed halide perovskite solar cells prepared by redissolution and crystal grain growth via spray coating. *J. Mater. Chem. A* **4**, 17636–17642 (2016).
35. Mohamad, D. K., Griffin, J., Bracher, C., Barrows, A. T. & Lidzey, D. G. Spray-cast multilayer organometal perovskite solar cells fabricated in air. *Adv. Energy Mater.* **6**, 1600994 (2016).
36. Hong, S. C. et al. Precise morphology control and continuous fabrication of perovskite solar cells using droplet-controllable electrospray coating system. *ACS Appl. Mater. Interfaces* **7**, 7879–7884 (2017).
37. Li, S.G. et al. Inkjet printing of CH₃NH₃PbI₃ on a mesoscopic TiO₂ film for highly efficient perovskite solar cells. *J. Mater. Chem. A* **3**, 9092–9097 (2015).
38. Bao, Z., Rogers, A., J & Katz, E. H. Printable organic and polymeric semiconducting materials and devices. *J. Mater. Chem.* **9**, 1895–1904 (1999).
39. Mei, A. et al. A hole-conductor–free, fully printable mesoscopic perovskite solar cell with high stability. *Science* **345**, 295–298 (2014).
   Report on screen-printed PSCs with porous carbon electrodes showing outstanding device stability.
40. Koza, J. A., Hill, J. C., Demster, A. C. & Switzer, J. A. Epitaxial electrodeposition of methylammonium lead iodide perovskites. *Chem. Mater.* **28**, 399–405 (2016).
41. Chen, H., Wei, Z., Zheng, X. & Yang, S. A scalable electrodeposition route to the low-cost, versatile and controllable fabrication of perovskite solar cells. *Nano Energy* **15**, 216–226 (2015).
42. Cui, X. P. et al. Electrodeposition of PbO and its in situ conversion to CH₃NH₃PbI₃ for mesoscopic perovskite solar cells. *Chem. Commun* **51**, 1457–1460 (2015).
43. Huang, J. H. et al. Direct conversion of CH₃NH₃PbI₃ from electrodeposited PbO for highly efficient planar perovskite solar cells. *Sci. Rep.* **5**, 15889 (2015).
44. Popov, G., Mattinen, M., Kemell, M. L., Ritala, M. & Leskelä, M. Scalable route to the fabrication of CH₃NH₃PbI₃ perovskite thin films by electrodeposition and vapor conversion. *ACS Omega* **1**, 1296–1306 (2016).
45. Lee, J.W., Na, S.I. & Kim, S.S. Efficient spin-coating-free planar heterojunction perovskite solar cells fabricated with successive brush-painting. *J. Power Sources* **339**, 33–40 (2017).
46. Liao, H.C. et al. Enhanced efficiency of hot-cast large-area planar perovskite solar cells/modules having controlled chloride incorporation. *Adv. Energy Mater.* **7**, 1601660 (2017).
47. Gao, L.L., Li, C.X., Li, C.J. & Yang, G.J. Large-area high-efficiency perovskite solar cells based on perovskite films dried by the multi-flow air knife method in air. *J. Mater. Chem. A* **5**, 1548–1557 (2017).
48. Liu, M., Johnston, M. B. & Snaith, H. J. Efficient planar heterojunction perovskite solar cells by vapour deposition. *Nature* **501**, 395–398 (2013).
49. Ono, L. K., Wang, S., Kato, Y., Raga, S. R. & Qi, Y. Fabrication of semi-transparent perovskite films with centimeter-scale superior uniformity by the hybrid deposition method. *Energy Environ. Sci.* **7**, 3989–3993 (2014).
50. Forgács, D. et al. Efficient monolithic perovskite/perovskite tandem solar cells. *Adv. Energy Mater.* **7**, 1602121 (2017).
51. Chen, Q. et al. Planar heterojunction perovskite solar cells via vapor-assisted solution process. *J. Am. Chem. Soc.* **136**, 622–625 (2014).
52. Leyden, M. R., Lee, M. V., Raga, S. R. & Qi, Y. Large formamidinium lead trihalide perovskite solar cells using chemical vapor deposition with high reproducibility and tunable chlorine concentrations. *J. Mater. Chem. A* **3**, 16097–16103 (2015).
53. Luo, P. et al. A simple in situ tubular chemical vapor deposition processing of large-scale efficient perovskite solar cells and the research on their novel roll-over phenomenon in J–V curves. *J. Mater. Chem. A* **3**, 12443–12451 (2015).
54. Todorov, T. et al. Monolithic perovskite-CIGS tandem solar cells via in situ band gap engineering. *Adv. Energy Mater.* **5**, 1500799 (2015).
55. Guo, Y. et al. Chemical pathways connecting lead(II) iodide and perovskite via polymeric plumbate(II) fiber. *J. Am. Chem. Soc.* **137**, 15907–15914 (2015).
56. Xiao, M. et al. A fast deposition-crystallization procedure for highly efficient lead iodide perovskite thin-film solar cells. *Angew. Chem. Int. Ed.* **53**, 9898–9903 (2014).
57. Zhou, Y. et al. Room-temperature crystallization of hybrid-perovskite thin films via solvent–solvent extraction for high-performance solar cells. *J. Mater. Chem. A* **3**, 8178–8184 (2015).
58. Nie, W. et al. High-efficiency solution-processed perovskite solar cells with millimeter-scale grains. *Science* **347**, 522–525 (2015).

59. Deng, Y. et al. Scalable fabrication of efficient organolead trihalide perovskite solar cells with doctor-bladed active layers. *Energy Environ. Sci.* **8**, 1544–1550 (2015).

60. Huang, F. et al. Gas-assisted preparation of lead iodide perovskite films consisting of a monolayer of single crystalline grains for high efficiency planar solar cells. *Nano Energy* **10**, 10–18 (2014).

61. Cotella, G. et al. One-step deposition by slot-die coating of mixed lead halide perovskite for photovoltaic applications. *Sol. Energy Mater. Sol. Cells* **159**, 362–369 (2017).

62. Li, X. et al. A vacuum flash–assisted solution process for high-efficiency large-area perovskite solar cells. *Science* **353**, 58–62 (2016).
   Study in which vacuum is used to assist rapid solvent removal and fabricate large-area PSCs with high PCE.

63. Ding, B. et al. Facile and scalable fabrication of highly efficient lead iodide perovskite thin-film solar cells in air using gas pump method. *ACS Appl. Mater. Interfaces* **8**, 20067–20073 (2016).

64. Gao, L.L. et al. Preparation of flexible perovskite solar cells by a gas pump drying method on a plastic substrate. *J. Mater. Chem. A* **4**, 3704–3710 (2016).

65. Ding, B. et al. Material nucleation/growth competition tuning towards highly reproducible planar perovskite solar cells with efficiency exceeding 20%. *J. Mater. Chem. A* **5**, 6840–6848 (2017).

66. Yin, M. et al. Annealing-free perovskite films by instant crystallization for efficient solar cells. *J. Mater. Chem. A* **4**, 8548–8553 (2016).

67. Yu, Y. et al. Ultrasmooth perovskite film via mixed anti-solvent strategy with improved efficiency. *ACS Appl. Mater. Interfaces* **9**, 3667–3676 (2017).

68. Eperon, G. E. et al. Perovskite-perovskite tandem photovoltaics with optimized band gaps. *Science* **354**, 861–865 (2016).

69. Ye, J. et al. Enhanced morphology and stability of high-performance perovskite solar cells with ultra-smooth surface and high fill factor via crystal growth engineering. *Sustain. Energy Fuels* **1**, 907–914 (2017).

70. Kim, J. et al. Overcoming the challenges of large-area high-efficiency perovskite solar cells. *ACS Energy Lett.* **2**, 1978–1984 (2017).

71. Deng, Y., Dong, Q., Bi, C., Yuan, Y. & Huang, J. Air-stable, efficient mixed-cation perovskite solar cells with Cu electrode by scalable fabrication of active layer. *Adv. Energy Mater.* **6**, 1600372 (2016).

72. Ye, F. et al. Low-temperature soft-cover deposition of uniform large-scale perovskite films for high-performance solar cells. *Adv. Mater.* **29**, 1701440 (2017).

73. Noel, N. K. et al. A low viscosity, low boiling point, clean solvent system for the rapid crystallisation of highly specular perovskite films. *Energy Environ. Sci.* **10**, 145–152 (2017).

74. Zhou, Z. et al. Methylamine-gas-induced defect-healing behavior of $CH_3NH_3PbI_3$ thin films for perovskite solar cells. *Angew. Chem. Int. Ed.* **54**, 9705–9709 (2015).

75. Lee, M. M., Teuscher, J., Miyasaka, T., Murakami, T. N. & Snaith, H. J. Efficient hybrid solar cells based on meso-superstructured organometal halide perovskites. *Science* **338**, 643–647 (2012).

76. Zhao, Y. & Zhu, K. CH_3NH_3Cl-assisted one-step solution growth of $CH_3NH_3PbI_3$: structure, charge-carrier dynamics, and photovoltaic properties of perovskite solar cells. *J. Phys. Chem. C* **118**, 9412–9418 (2014).

77. Zuo, C. & Ding, L. An 80.11% FF record achieved for perovskite solar cells by using the NH_4Cl additive. *Nanoscale* **6**, 9935–9938 (2014).

78. Chen, Y., Zhao, Y. & Liang, Z. Non-thermal annealing fabrication of efficient planar perovskite solar cells with inclusion of NH_4Cl. *Chem. Mater.* **27**, 1448–1451 (2015).

79. Krautscheid, H. & Vielsack, F. Discrete and polymeric iodoplumbates with Pb_3I_{10} building blocks: $[Pb_3I_{10}]^{4-}$, $[Pb_7I_{22}]^{8-}$, $[Pb_{10}I_{28}]^{8-}$, $^1_\infty[Pb_3I_{10}]^{4-}$ and $^2_\infty[Pb_7I_{18}]^{4-}$. *J. Chem. Soc., Dalton Trans.*, 2731–2735 (1999).

80. Yantara, N. et al. Unravelling the effects of Cl addition in single step $CH_3NH_3PbI_3$ perovskite solar cells. *Chem. Mater.* **27**, 2309–2314 (2015).

81. Yu, H. et al. The role of chlorine in the formation process of "$CH_3NH_3PbI_{3-x}Cl_x$" perovskite. *Adv. Funct. Mater.* **24**, 7102–7108 (2014).

82. Barrows, A. T. et al. Efficient planar heterojunction mixed-halide perovskite solar cells deposited via spray-deposition. *Energy Environ. Sci.* **7**, 2944–2950 (2014).

83. Yang, Z. et al. High-performance fully printable perovskite solar cells via blade-coating technique under the ambient condition. *Adv. Energy Mater.* **5**, 1500328 (2015).

84. Schmidt, T. M., Larsen-Olsen, T. T., Carlé, J. E., Angmo, D. & Krebs, F. C. Upscaling of perovskite solar cells: fully ambient roll processing of flexible perovskite solar cells with printed back electrodes. *Adv. Energy Mater.* **5**, 1500569 (2015).

85. Yang, M. et al. Square-centimeter solution-processed planar $CH_3NH_3PbI_3$ perovskite solar cells with efficiency exceeding 15%. *Adv. Mater.* **27**, 6363–6370 (2015).

86. Zhang, W. et al. Ultrasmooth organic–inorganic perovskite thin-film formation and crystallization for efficient planar heterojunction solar cells. *Nat. Commun.* **6**, 6142 (2015).

87. Moore, D. T. et al. Crystallization kinetics of organic–inorganic trihalide perovskites and the role of the lead anion in crystal growth. *J. Am. Chem. Soc.* **137**, 2350–2358 (2015).
   This article provides an examination of the mechanisms of crystal-growth control through the addition of chemical additives to perovskite precursor solutions.

88. Li, G. et al. Ion-exchange-induced 2D – 3D conversion of $HMA_{1-x}FA_xPbI_3Cl$ perovskite into a high-quality $MA_{1-x}FA_xPbI_3$ perovskite. *Angew. Chem. Int. Ed.* **55**, 13460–13464 (2016).

89. Li, G., Zhang, T. & Zhao, Y. Hydrochloric acid accelerated formation of planar $CH_3NH_3PbI_3$ perovskite with high humidity tolerance. *J. Mater. Chem. A* **3**, 19674–19678 (2015).

90. Pan, J. et al. Room-temperature, hydrochloride-assisted, one-step deposition for highly efficient and air-stable perovskite solar cells. *Adv. Mater.* **28**, 8309–8314 (2016).

91. Heo, J. H., Song, D. H. & Im, S. H. Planar $CH_3NH_3PbBr_3$ hybrid solar cells with 10.4% power conversion efficiency, fabricated by controlled crystallization in the spin-coating process. *Adv. Mater.* **26**, 8179–8183 (2014).

92. Heo, J. H. et al. Planar $CH_3NH_3PbI_3$ perovskite solar cells with constant 17.2% average power conversion efficiency irrespective of the scan rate. *Adv. Mater.* **27**, 3424–3430 (2015).

93. Nayak, P. K. et al. Mechanism for rapid growth of organic–inorganic halide perovskite crystals. *Nat. Commun.* **7**, 13303 (2016).

94. Lewis, G. N. Acids and bases. *J. Franklin Inst.* **226**, 293–313 (1938).

95. Lee, J. W., Kim, H. S. & Park, N. G. Lewis acid–base adduct approach for high efficiency perovskite solar cells. *Acc. Chem. Res.* **49**, 311–319 (2016).
   This study demonstrates that Lewis bases can form complexes with perovskites and change the perovskite film morphology.

96. Jeon, Y. J. et al. Planar heterojunction perovskite solar cells with superior reproducibility. *Sci. Rep.* **4**, 6953 (2014).

97. Zhang, Y. et al. PbI_2–HMPA complex pretreatment for highly reproducible and efficient $CH_3NH_3PbI_3$ perovskite solar cells. *J. Am. Chem. Soc.* **138**, 14380–14387 (2016).

98. Liang, P. W. et al. Additive enhanced crystallization of solution-processed perovskite for highly efficient planar-heterojunction solar cells. *Adv. Mater.* **26**, 3748–3754 (2014).

99. Wu, Y. et al. Thermally stable $MAPbI_3$ perovskite solar cells with efficiency of 19.19% and area over 1 cm² achieved by additive engineering. *Adv. Mater.* **29**, 1701073 (2017).

100. Wang, Z. K. et al. Induced crystallization of perovskites by a perylene underlayer for high-performance solar cells. *ACS Nano* **10**, 5479–5489 (2016).

101. Gu, Z. et al. Interfacial engineering of self-assembled monolayer modified semi-roll-to-roll planar heterojunction perovskite solar cells on flexible substrates. *J. Mater. Chem. A* **3**, 24254–24260 (2015).

102. Li, B., Chen, Y., Liang, Z., Gao, D. & Huang, W. Interfacial engineering by using self-assembled monolayer in mesoporous perovskite solar cell. *RSC Adv.* **5**, 94290–94295 (2015).

103. Ding, Y., Yao, X., Zhang, X., Wei, C. & Zhao, Y. Surfactant enhanced surface coverage of $CH_3NH_3PbI_{3-x}Cl_x$ perovskite for highly efficient mesoscopic solar cells. *J. Power Sources* **272**, 351–355 (2014).

104. Bi, C. et al. Non-wetting surface-driven high-aspect-ratio crystalline grain growth for efficient hybrid perovskite solar cells. *Nat. Commun.* **6**, 7747 (2015).

105. Burschka, J. et al. Sequential deposition as a route to high-performance perovskite-sensitized solar cells. *Nature* **499**, 316–319 (2013).

106. Hwang, K. et al. Toward large scale roll-to-roll production of fully printed perovskite solar cells. *Adv. Mater.* **27**, 1241–1247 (2015).

107. Huang, H. et al. Two-step ultrasonic spray deposition of $CH_3NH_3PbI_3$ for efficient and large-area perovskite solar cell. *Nano Energy* **27**, 352–358 (2016).

108. Chandrasekhar, P. S., Kumar, N., Swami, S. K., Dutta, V. & Komarala, V. K. Fabrication of perovskite films using an electrostatic assisted spray technique: the effect of the electric field on morphology, crystallinity and solar cell performance. *Nanoscale* **8**, 6792–6800 (2016).

109. Xia, X. et al. Spray reaction prepared $FA_{1-x}Cs_xPbI_3$ solid solution as a light harvester for perovskite solar cells with improved humidity stability. *RSC Adv.* **6**, 14792–14798 (2016).

110. Remeika, M., Raga, S. R., Zhang, S. & Qi, Y. Transferrable optimization of spray-coated PbI_2 films for perovskite solar cell fabrication. *J. Mater. Chem. A* **5**, 5709–5718 (2017).

111. Tai, Q. et al. Efficient and stable perovskite solar cells prepared in ambient air irrespective of the humidity. *Nat. Commun.* **7**, 11105 (2016).

112. Ko, H.S., Lee, J.W. & Park, N.G. 15.76% efficiency perovskite solar cells prepared under high relative humidity: importance of PbI_2 morphology in two-step deposition of $CH_3NH_3PbI_3$. *J. Mater. Chem. A* **3**, 8808–8815 (2015).

113. Chiang, C.H., Nazeeruddin, M. K., Grätzel, M. & Wu, C.G. The synergistic effect of H_2O and DMF towards stable and 20% efficiency inverted perovskite solar cells. *Energy Environ. Sci.* **10**, 808–817 (2017).

114. Yang, W. S. et al. High-performance photovoltaic perovskite layers fabricated through intramolecular exchange. *Science* **348**, 1234–1237 (2015).

115. Cao, X. et al. Enhanced performance of perovskite solar cells by modulating the Lewis acid–base reaction. *Nanoscale* **8**, 19804–19810 (2016).

116. Jo, Y. et al. High performance of planar perovskite solar cells produced from $PbI_2(DMSO)$ and $PbI_2(NMP)$ complexes by intramolecular exchange. *Adv. Mater. Interfaces* **3**, 1500768 (2016).

117. Cao, X. et al. Control of the morphology of PbI_2 films for efficient perovskite solar cells by strong Lewis base additives. *J. Mater. Chem. C* **5**, 7458–7464 (2017).

118. Zhang, H. et al. Toward all room-temperature, solution-processed, high-performance planar perovskite solar cells: a new scheme of pyridine-promoted perovskite formation. *Adv. Mater.* **29**, 1604695 (2017).

119. Zhang, H. et al. A smooth $CH_3NH_3PbI_3$ film via a new approach for forming the PbI_2 nanostructure together with strategically high CH_3NH_3I concentration for high efficient planar-heterojunction solar cells. *Adv. Energy Mater.* **5**, 1501354 (2015).

120. Zhang, T., Yang, M., Zhao, Y. & Zhu, K. Controllable sequential deposition of planar $CH_3NH_3PbI_3$ perovskite films via adjustable volume expansion. *Nano Lett.* **15**, 3959–3963 (2015).

121. Troughton, J. et al. Rapid processing of perovskite solar cells in under 2.5 seconds. *J. Mater. Chem. A* **3**, 9123–9127 (2015).

122. Troughton, J. et al. Photonic flash-annealing of lead halide perovskite solar cells in 1ms. *J. Mater. Chem. A* **4**, 3471–3476 (2016).

123. Druffel, T., Dharmadasa, R., Lavery, B. W. & Ankireddy, K. Intense pulsed light processing for photovoltaic manufacturing. *Sol. Energy Mater. Sol. Cells* **174**, 359–369 (2018).

124. Pool, V. L. et al. Thermal engineering of $FAPbI_3$ perovskite material via radiative thermal annealing and in situ XRD. *Nat. Commun.* **8**, 14075 (2017).

125. Yang, M. et al. Facile fabrication of large-grain $CH_3NH_3PbI_{3-x}Br_x$ films for high-efficiency solar cells via CH_3NH_3Br-selective Ostwald ripening. *Nat. Commun.* **7**, 12305 (2016).

126. Xiao, Z. et al. Solvent annealing of perovskite-induced crystal growth for photovoltaic-device efficiency enhancement. *Adv. Mater.* **26**, 6503–6509 (2014).

127. You, J. et al. Moisture assisted perovskite film growth for high performance solar cells. *Appl. Phys. Lett.* **105**, 183902 (2014).

128. Liu, C. et al. Efficient perovskite hybrid photovoltaics via alcohol-vapor annealing treatment. *Adv. Funct. Mater.* **26**, 101–110 (2016).

129. Liu, J. et al. Improved crystallization of perovskite films by optimized solvent annealing for high efficiency solar cell. *ACS Appl. Mater. Interfaces* **7**, 24008–24015 (2015).

130. Gouda, L. et al. Vapor and healing treatment for $CH_3NH_3PbI_{3−x}Cl_x$ films toward large-area perovskite solar cells. *Nanoscale* **8**, 6386–6392 (2016).

131. Jiang, Y. et al. Post-annealing of MAPbI$_3$ perovskite films with methylamine for efficient perovskite solar cells. *Mater. Horiz.* **3**, 548–555 (2016).

132. Jain, S. M. et al. Frustrated Lewis pair-mediated recrystallization of $CH_3NH_3PbI_3$ for improved optoelectronic quality and high voltage planar perovskite solar cells. *Energy Environ. Sci.* **9**, 3770–3782 (2016).

133. Kim, H.S. et al. High efficiency solid-state sensitized solar cell-based on submicrometer rutile TiO$_2$ nanorod and $CH_3NH_3PbI_3$ perovskite sensitizer. *Nano Lett.* **13**, 2412–2417 (2013).

134. Ke, W. et al. Low-temperature solution-processed tin oxide as an alternative electron transporting layer for efficient perovskite solar cells. *J. Am. Chem. Soc.* **137**, 6730–6733 (2015).

135. Liu, D. & Kelly, T. L. Perovskite solar cells with a planar heterojunction structure prepared using room-temperature solution processing techniques. *Nat. Photon.* **8**, 133–138 (2014).

136. Jeon, N. J. et al. *o*-Methoxy substituents in spiro-OMeTAD for efficient inorganic–organic hybrid perovskite solar cells. *J. Am. Chem. Soc.* **136**, 7837–7840 (2014).

137. Heo, J. H. et al. Efficient inorganic–organic hybrid heterojunction solar cells containing perovskite compound and polymeric hole conductors. *Nat. Photon.* **7**, 486–491 (2013).

138. Christians, J. A., Fung, R. C. M. & Kamat, P. V. An inorganic hole conductor for organo-lead halide perovskite solar cells. Improved hole conductivity with copper iodide. *J. Am. Chem. Soc.* **136**, 758–764 (2014).

139. Qin, P. et al. Inorganic hole conductor-based lead halide perovskite solar cells with 12.4% conversion efficiency. *Nat. Commun.* **5**, 3834 (2014).

140. Jeng, J.Y. et al. $CH_3NH_3PbI_3$ perovskite/fullerene planar-heterojunction hybrid solar cells. *Adv. Mater.* **25**, 3727–3732 (2013).

141. Wang, Q. et al. Large fill-factor bilayer iodine perovskite solar cells fabricated by a low-temperature solution-process. *Energy Environ. Sci.* **7**, 2359–2365 (2014).

142. Jeng, J.Y. et al. Nickel oxide electrode interlayer in $CH_3NH_3PbI_3$ perovskite/PCBM planar-heterojunction hybrid solar cells. *Adv. Mater.* **26**, 4107–4113 (2014).

143. Ye, S. et al. CuSCN-based inverted planar perovskite solar cell with an average PCE of 15.6%. *Nano Lett.* **15**, 3723–3728 (2015).

144. Chen, C., Cheng, Y., Dai, Q. & Song, H. Radio frequency magnetron sputtering deposition of TiO$_2$ thin films and their perovskite solar cell applications. *Sci. Rep.* **5**, 17684 (2015).

145. Ke, W. et al. Perovskite solar cell with an efficient TiO$_2$ compact film. *ACS Appl. Mater. Interfaces* **6**, 15959–15965 (2014).

146. Qiu, W. et al. An electron beam evaporated TiO$_2$ layer for high efficiency planar perovskite solar cells on flexible polyethylene terephthalate substrates. *J. Mater. Chem. A* **3**, 22824–22829 (2015).

147. Wu, Y. et al. Highly compact TiO$_2$ layer for efficient hole-blocking in perovskite solar cells. *Appl. Phys. Expr.* **7**, 052301 (2014).

148. Di Giacomo, F. et al. Flexible perovskite photovoltaic modules and solar cells based on atomic layer deposited compact layers and UV-irradiated TiO$_2$ scaffolds on plastic substrates. *Adv. Energy Mater.* **5**, 1401808 (2015).

149. Yella, A., Heiniger, L.P., Gao, P., Nazeeruddin, M. K. & Grätzel, M. Nanocrystalline rutile electron extraction layer enables low-temperature solution processed perovskite photovoltaics with 13.7% efficiency. *Nano Lett.* **14**, 2591–2596 (2014).

150. Fakharuddin, A. et al. Vertical TiO$_2$ nanorods as a medium for stable and high-efficiency perovskite solar modules. *ACS Nano* **9**, 8420–8429 (2015).

151. Su, T. S., Hsieh, T. Y., Hong, C. Y. & Wei, T. C. Electrodeposited ultrathin TiO$_2$ blocking layers for efficient perovskite solar cells. *Sci. Rep.* **5**, 16098 (2015).

152. Correa Baena, J. P. et al. Highly efficient planar perovskite solar cells through band alignment engineering. *Energy Environ. Sci.* **8**, 2928–2934 (2015).

153. Anaraki, E. H. et al. Highly efficient and stable planar perovskite solar cells by solution-processed tin oxide. *Energy Environ. Sci.* **9**, 3128–3134 (2016).

154. Zhu, Z. et al. Enhanced efficiency and stability of inverted perovskite solar cells using highly crystalline SnO$_2$ nanocrystals as the robust electron-transporting layer. *Adv. Mater.* **28**, 6478–6484 (2016).

155. Chen, J.Y., Chueh, C.C., Zhu, Z., Chen, W.C. & Jen, A. K. Y. Low-temperature electrodeposited crystalline SnO$_2$ as an efficient electron-transporting layer for conventional perovskite solar cells. *Sol. Energy Mater. Sol. Cells* **164**, 47–55 (2017).

156. You, J. et al. Improved air stability of perovskite solar cells via solution-processed metal oxide transport layers. *Nat. Nanotechnol.* **11**, 75–81 (2016).

157. Chen, W. et al. Hybrid interfacial layer leads to solid performance improvement of inverted perovskite solar cells. *Energy Environ. Sci.* **8**, 629–640 (2015).

158. Zhu, Z. et al. High-performance hole-extraction layer of sol–gel-processed NiO nanocrystals for inverted planar perovskite solar cells. *Angew. Chem. Int. Ed.* **53**, 12571–12575 (2014).

159. Seo, S. et al. An ultra-thin, undoped NiO hole transporting layer of highly efficient (16.4%) organic–inorganic hybrid perovskite solar cells. *Nanoscale* **8**, 11403–11412 (2016).

160. Wang, K. C. et al. Low-temperature sputtered nickel oxide compact thin film as effective electron blocking layer for mesoscopic NiO/$CH_3NH_3PbI_3$ perovskite heterojunction solar cells. *ACS Appl. Mater. Interfaces* **6**, 11851–11858 (2014).

161. Park, I. J. et al. Highly efficient and uniform 1 cm^2 perovskite solar cells with an electrochemically deposited NiO$_x$ hole-extraction layer. *ChemSusChem* **10**, 2660–2667 (2017).

162. Zhang, H. et al. Pinhole-free and surface-nanostructured NiO$_x$ film by room-temperature solution process for high-performance flexible perovskite solar cells with good stability and reproducibility. *ACS Nano* **10**, 1503–1511 (2016).

163. Hou, Y. et al. Overcoming the interface losses in planar heterojunction perovskite-based solar cells. *Adv. Mater.* **28**, 5112–5120 (2016).

164. Yang, I. S. et al. Formation of pristine CuSCN layer by spray deposition method for efficient perovskite solar cell with extended stability. *Nano Energy* **32**, 414–421 (2017).

165. Qin, T. et al. Amorphous hole-transporting layer in slot-die coated perovskite solar cells. *Nano Energy* **31**, 210–217 (2017).

166. Fu, F. et al. Low-temperature-processed efficient semi-transparent planar perovskite solar cells for bifacial and tandem applications. *Nat. Commun.* **6**, 8932 (2015).

167. Bush, K. A. et al. Thermal and environmental stability of semi-transparent perovskite solar cells for tandems enabled by a solution-processed nanoparticle buffer layer and sputtered ITO electrode. *Adv. Mater.* **28**, 3937–3943 (2016).

168. Chang, C.Y., Lee, K.T., Huang, W.K., Siao, H.Y. & Chang, Y.C. High-performance, air-stable, low-temperature processed semitransparent perovskite solar cells enabled by atomic layer deposition. *Chem. Mater.* **27**, 5122–5130 (2015).

169. Bryant, D. et al. A transparent conductive adhesive laminate electrode for high-efficiency organic-inorganic lead halide perovskite solar cells. *Adv. Mater.* **26**, 7499–7504 (2014).

170. Wei, Z. et al. Cost-efficient clamping solar cells using candle soot for hole extraction from ambipolar perovskites. *Energy Environ. Sci.* **7**, 3326–3333 (2014).

171. You, P., Liu, Z., Tai, Q., Liu, S. & Yan, F. Efficient semitransparent perovskite solar cells with graphene electrodes. *Adv. Mater.* **27**, 3632–3638 (2015).

172. Grancini, G. et al. One-year stable perovskite solar cells by 2D/3D interface engineering. *Nat. Commun.* **8**, 15684 (2017).

173. Hu, Y. et al. Stable large-area (10 × 10 cm^2) printable mesoscopic perovskite module exceeding 10% efficiency. *Solar RRL* **1**, 1600019 (2017).

174. Priyadarshi, A. et al. A large area (70 cm^2) monolithic perovskite solar module with a high efficiency and stability. *Energy Environ. Sci.* **9**, 3687–3692 (2016).

175. Niu, G., Guo, X. & Wang, L. Review of recent progress in chemical stability of perovskite solar cells. *J. Mater. Chem. A* **3**, 8970–8980 (2015).

176. Kim, H.S., Seo, J.Y. & Park, N.G. Material and device stability in perovskite solar cells. *ChemSusChem* **9**, 2528–2540 (2016).

177. Leijtens, T. et al. Towards enabling stable lead halide perovskite solar cells; interplay between structural, environmental, and thermal stability. *J. Mater. Chem. A* **5**, 11483–11500 (2017).

178. Yang, Y. & You, J. Make perovskite solar cells stable. *Nature* **544**, 155–156 (2017).

179. Christians, J. A. et al. Tailored interfaces of unencapsulated perovskite solar cells for > 1,000 hour operational stability. *Nat. Energy* **3**, 68–74 (2018).
   This study demonstrates the importance of the interfaces between the perovskite and charge-transport layers in determining the stability of PSCs.

180. Manser, J. S., Saidaminov, M. I., Christians, J. A., Bakr, O. M. & Kamat, P. V. Making and breaking of lead halide perovskites. *Accounts Chem. Res.* **49**, 330–338 (2016).

181. Pellet, N. et al. Mixed-organic-cation perovskite photovoltaics for enhanced solar-light harvesting. *Angew. Chem. Int. Ed.* **53**, 3151–3157 (2014).

182. Li, Z. et al. Stabilizing perovskite structures by tuning tolerance factor: formation of formamidinium and cesium lead iodide solid-state alloys. *Chem. Mater.* **28**, 284–292 (2016).

183. Saliba, M. et al. Incorporation of rubidium cations into perovskite solar cells improves photovoltaic performance. *Science* **354**, 206–209 (2016).

184. Jeon, N. J. et al. Compositional engineering of perovskite materials for high-performance solar cells. *Nature* **517**, 476–480 (2015).

185. Yang, S. et al. Functionalization of perovskite thin films with moisture-tolerant molecules. *Nat. Energy* **1**, 15016 (2016).

186. Wang, F. et al. Phenylalkylamine passivation of organolead halide perovskites enabling high-efficiency and air-stable photovoltaic cells. *Adv. Mater.* **28**, 9986–9992 (2016).

187. Tsai, H. et al. High-efficiency two-dimensional Ruddlesden–Popper perovskite solar cells. *Nature* **536**, 312–316 (2016).

188. Jiang, Q. et al. Enhanced electron extraction using SnO$_2$ for high-efficiency planar-structure $HC(NH_2)_2PbI_3$-based perovskite solar cells. *Nat. Energy* **2**, 16177 (2016).

189. Shin, S. S. et al. Colloidally prepared La-doped BaSnO$_3$ electrodes for efficient, photostable perovskite solar cells. *Science* **356**, 167–171 (2017).

190. Tan, H. et al. Efficient and stable solution-processed planar perovskite solar cells via contact passivation. *Science* **355**, 722–726 (2017).

191. Ono, L. K. et al. Pinhole-free hole transport layers significantly improve the stability of MAPbI$_3$-based perovskite solar cells under operating conditions. *J. Mater. Chem. A* **3**, 15451–15456 (2015).

192. Li, Z. et al. Extrinsic ion migration in perovskite solar cells. *Energy Environ. Sci.* **10**, 1234–1242 (2017).

193. Leijtens, T. et al. Hydrophobic organic hole transporters for improved moisture resistance in metal halide perovskite solar cells. *ACS Appl. Mater. Interfaces* **8**, 5981–5989 (2016).

194. Kim, G.W. et al. Dopant-free polymeric hole transport materials for highly efficient and stable perovskite solar cells. *Energy Environ. Sci.* **9**, 2326–2333 (2016).

195. Hou, Y. et al. A generic interface to reduce the efficiency-stability-cost gap of perovskite solar cells. *Science* **358**, 1192–1197 (2017).

196. Habisreutinger, S. N. et al. Carbon nanotube/polymer composites as a highly stable hole collection layer in perovskite solar cells. *Nano Lett.* **14**, 5561–5568 (2014).

197. Chen, W. et al. Efficient and stable large-area perovskite solar cells with inorganic charge extraction layers. *Science* **350**, 944–948 (2015).

198. Arora, N. et al. Perovskite solar cells with CuSCN hole extraction layers yield stabilized efficiencies greater than 20%. *Science* **358**, 768–771 (2017).

199. Kato, Y. et al. Silver iodide formation in methyl ammonium lead iodide perovskite solar cells with silver top electrodes. *Adv. Mater. Interfaces* **2**, 1500195 (2015).

200. Domanski, K. et al. Not all that glitters is gold: metal-migration-induced degradation in perovskite solar cells. *ACS Nano* **10**, 6306–6314 (2016).

201. Kaltenbrunner, M. et al. Flexible high power-per-weight perovskite solar cells with chromium oxide–metal contacts for improved stability in air. *Nat. Mater.* **14**, 1032–1039 (2015).

202. Sanehira, E. M. et al. Influence of electrode interfaces on the stability of perovskite solar cells: reduced degradation using MoO$_x$/Al for hole collection. *ACS Energy Lett.* **1**, 38–45 (2016).

203. Bella, F. et al. Improving efficiency and stability of perovskite solar cells with photocurable fluoropolymers. *Science* **354**, 203–206 (2016).

REVIEWS

204. Bauer, J. et al. Hot spots in multicrystalline silicon solar cells: avalanche breakdown due to etch pits. *Phys. Status Solidi RRL* **3**, 40–42 (2009).
205. Lee, J. E. et al. Investigation of damage caused by partial shading of $CuIn_xGa_{(1-x)}Se_2$ photovoltaic modules with bypass diodes. *Prog. Photovolt.* **24**, 1035–1043 (2016).
206. Rossander, L. H. et al. *In situ* X-ray scattering of perovskite solar cell active layers roll-to-roll coated on flexible substrates. *CrystEngComm* **18**, 5083–5088 (2016).
207. Razza, S. et al. Perovskite solar cells and large area modules (100 cm²) based on an air flow-assisted PbI_2 blade coating deposition process. *J. Power Sources* **277**, 286–291 (2015).
208. Song, Z. et al. Investigation of degradation mechanisms of perovskite-based photovoltaic devices using laser beam induced current mapping. *Proc. SPIE* **9561**, 956107 (2015).
209. Bi, D. et al. Efficient luminescent solar cells based on tailored mixed-cation perovskites. *Sci. Adv.* **2**, e1501170 (2016).
210. Tress, W. et al. Predicting the open-circuit voltage of $CH_3NH_3PbI_3$ perovskite solar cells using electroluminescence and photovoltaic quantum efficiency spectra: the role of radiative and non-radiative recombination. *Adv. Energy Mater.* **5**, 1400812 (2015).
211. Mastroianni, S. et al. Analysing the effect of crystal size and structure in highly efficient $CH_3NH_3PbI_3$ perovskite solar cells by spatially resolved photo- and electroluminescence imaging. *Nanoscale* **7**, 19653–19662 (2015).
212. Hameiri, Z. et al. Photoluminescence and electroluminescence imaging of perovskite solar cells. *Prog. Photovolt.* **23**, 1697–1705 (2015).
213. Soufiani, A. M. et al. Electro- and photoluminescence imaging as fast screening technique of the layer uniformity and device degradation in planar perovskite solar cells. *J. Appl. Phys.* **120**, 35702 (2016).
214. Walter, D. et al. On the use of luminescence intensity images for quantified characterization of perovskite solar cells: spatial distribution of series resistance. *Adv. Energy Mater.* **8**, 1701522 (2017).
215. El-Hajje, G. et al. Quantification of spatial inhomogeneity in perovskite solar cells by hyperspectral luminescence imaging. *Energy Environ. Sci.* **9**, 2286–2294 (2016).
216. Johnston, S. et al. Correlations of Cu(In, Ga)Se₂ imaging with device performance, defects, and microstructural properties. *J. Vac. Sci. Technol. A* **30**, 04111D (2012).
217. Gerber, A. et al. Advanced large area characterization of thin-film solar modules by electroluminescence and thermography imaging techniques. *Sol. Energy Mater. Sol. Cells* **135**, 35–42 (2015).
218. Song, Z. et al. A technoeconomic analysis of perovskite solar module manufacturing with low-cost materials and techniques. *Energy Environ. Sci.* **10**, 1297–1305 (2017).
219. Cai, M. et al. Cost-performance analysis of perovskite solar modules. *Adv. Sci.* **4**, 1600269 (2017).
220. Chang, N. L. et al. A manufacturing cost estimation method with uncertainty analysis and its application to perovskite on glass photovoltaic modules. *Prog. Photovolt.* **25**, 390–405 (2017).
221. Gong, J., Darling, S. B. & You, F. Perovskite photovoltaics: life-cycle assessment of energy and environmental impacts. *Energy Environ. Sci.* **8**, 1953–1968 (2015).
222. Zhao, Y., Nardes, A. M. & Zhu, K. Effective hole extraction using MoO_x/Al contact in perovskite $CH_3NH_3PbI_3$ solar cells. *Appl. Phys. Lett.* **104**, 213906 (2014).
223. Kim, J. H., Williams, S. T., Cho, N., Chueh, C.C. & Jen, A. K. Y. Enhanced environmental stability of planar heterojunction perovskite solar cells based on blade-coating. *Adv. Energy Mater.* **5**, 1401229 (2015).
224. Kim, M. C. et al. Electro-spray deposition of a mesoporous TiO_2 charge collection layer: toward large scale and continuous production of high efficiency perovskite solar cells. *Nanoscale* **7**, 20725–20733 (2015).
225. Mathies, F. et al. Multipass inkjet printed planar methylammonium lead iodide perovskite solar cells. *J. Mater. Chem. A* **4**, 19207–19213 (2016).
226. Xu, X. et al. Hole selective NiO contact for efficient perovskite solar cells with carbon electrode. *Nano Lett.* **15**, 2402–2408 (2015).
227. Rong, Y. et al. Synergy of ammonium chloride and moisture on perovskite crystallization for efficient printable mesoscopic solar cells. *Nat. Commun.* **8**, 14555 (2017).
228. Liou, Y.J., Hsiao, P.T., Chen, L.C., Chu, Y.Y. & Teng, H. Structure and electron-conducting ability of TiO_2 films from electrophoretic deposition and paste-coating for dye-sensitized solar cells. *J. Phys. Chem. C* **115**, 25580–25589 (2011).
229. Wang, X. et al. TiO_2 nanotube arrays based flexible perovskite solar cells with transparent carbon nanotube electrode. *Nano Energy* **11**, 728–735 (2015).
230. Wu, Y. et al. Perovskite solar cells with 18.21% efficiency and area over 1 cm² fabricated by heterojunction engineering. *Nat. Energy* **1**, 16148 (2016).
231. Microquanta. Microquanta updated the record of perovskite module efficiency to 16%. *Microquanta* http://2107081062.wezhan.us/newsitem/277909853 (2017).

Author contributions
Z.L. and K.Z. researched data for the article. Z.L., K.Z. and J.J.B. wrote the article. All authors made a substantial contribution to the discussion of the content and reviewed and edited the manuscript before submission.

Competing interests
The authors declare no competing interests.

Publisher's note
Springer Nature remains neutral with regard to jurisdictional claims in published maps and institutional affiliations

How to cite this article
Li, Z. et al. Scalable fabrication of perovskite solar cells. *Nat. Rev. Mater.* **3**, 18017 (2018).